

# Chapter 6

## Examples of Constitutive Equations for Various Materials

In Chaps. 3 and 5 various constitutive equations to characterize behavior of materials at high temperature are presented. These equations include a number of material dependent parameters like Young's modulus, creep exponent, hardening modulus etc., to be identified from experimental data. Furthermore functions of stress, strain rate and temperature (sometimes called response functions) are unknown in advance and should be formulated according to available experimental data for given ranges of loading and specific material.

This chapter presents several examples of constitutive equations, response functions of stress and temperature as well as material parameters for selected engineering materials. In order to find a set of material parameters, uni-axial tests under constant temperature leading to homogeneous stress and deformation states are required. The majority of available experimental data is presented as tensile curves (stress-strain curves) and creep curves (creep strain vs. time curves) obtained from standard uni-axial tests. Based on such curves the response functions and material parameters are identified.

Section 6.1 provides an overview of approaches to calibrate constitutive models against experimental data of high-temperature material behavior. In Sect. 6.2 constitutive equations of isotropic high-temperature plasticity of several alloys are presented. The objective of Sect. 6.3 is to discuss anisotropic inelastic behavior. Two examples of initially anisotropic materials including a forged aluminium alloy and a multi-pass weld metal from an advanced steel are presented.

### 6.1 Basic Approaches of Identification

The problem to identify the material parameters (also known as the inverse problem) can be solved with the following steps

- Formulate the functional with respect to the unknown material parameters by the use of the (weighted) least squares method,
- Minimize the functional by specifying appropriate guess for the material parameters.

For simplified constitutive equations, e.g. power law creep or deformation plasticity, the above steps are enough to fit the deformation response with a desired accuracy. Various examples for applications of least square methods to compute material parameters in constitutive equations of creep are presented in Boyle and Spence (1983). Mathematical and numerical aspects of identification procedures are discussed in Mahnken and Stein (1996, 1997), among others.

In contrast, the identification of material properties in unified constitutive models to capture several phenomena of inelastic deformation like hardening/recovery, softening and damage under different loading paths can be ill-posed for the following reasons

- The unified model should be calibrated for wide strain rate, stress and temperature ranges to capture both creep and LCF regimes. For example, for cast iron materials the inelastic strain rate ranges from  $10^{-7}$  to 10 1/h (Längler et al. 2014). Therefore, not only the material parameters but also functions of strain rate, stress and temperature are unknown in advance and should be found during the identification process,
- The resolution of experimental data is usually not fine enough to perform a stable minimization. For example, inelastic strain rates at the beginning of the creep process after the loading are usually not well defined,
- Experimental data may show a large scatter generated by testing a series of specimens removed from the same material. The origins of scatter in creep tests are discussed, for example, in Dyson (1996),
- Inelastic behavior may significantly depend on the kind of processing of specimens, e.g. the heat treatment. As a result, different data sets for the material with the same chemical composition may be found in the literature. For example, one may compare experimental data for 9Cr1Mo (P91) ferritic steel obtained in different laboratories (Abe 2001; Choudhary et al. 2001; Eggeler et al. 1994; Kloc et al. 2001; Orlová et al. 1998; Wu et al. 2004).

An alternative approach is to develop a step-by-step identification procedure. For example, one may develop the identification procedure based on the following steps

- Experimental creep curves (creep strain versus time curves) are smoothed and transformed to the creep rate versus creep strain curves,
- Initial and minimum inelastic strain rates as functions of stress and temperature are processed from experimental data for creep and tensile regimes,
- Response functions of stress and temperature are identified from experimental data on initial and steady strain rates,
- Evolution equations for softening, ageing and damage are calibrated against experimental creep rate versus creep strain curves within the tertiary creep range

Step-by-step identification procedures are presented in Samir et al. (2005), Kostenko et al. (2006, 2009a), Längler et al. (2014), Naumenko and Gariboldi (2014), among others. An example will be presented in Sect. 6.2.3.

## 6.2 Isotropic Materials

In this section examples of constitutive equations for isotropic high-temperature behavior of several alloys are presented. Sections 6.2.1 and 6.2.2 provide simplified creep-damage constitutive equations. Here the hardening processes are ignored and the tertiary creep is described by a single damage variable. In Sects. 6.2.3 and 6.2.4 mechanisms-based models are discussed in detail. Examples of evolution equations for hardening/recovery, softening and ageing are presented. In all examples response functions of stress and temperature as well as values of material parameters are presented.

### 6.2.1 Type 316 Steel

The first example is type 316 stainless steel at 650 °C. In Liu et al. (1994) the following creep equations are applied

$$\begin{aligned} \dot{\boldsymbol{\varepsilon}}^{\text{pl}} &= \frac{3}{2} f_1(\sigma_{\text{VM}}) g_1(\omega) \frac{\boldsymbol{s}}{\sigma_{\text{VM}}}, \quad \dot{\omega} = f_2 \left[ \sigma_{\text{eq}}^\omega(\boldsymbol{\sigma}) \right] g_2(\omega), \\ \boldsymbol{\varepsilon}^{\text{pl}}|_{t=0} &= \mathbf{0}, \quad \omega|_{t=0} = 0, \quad 0 \leq \omega \leq \omega_*, \\ \boldsymbol{s} &= \boldsymbol{\sigma} - \frac{1}{3} \text{tr} \boldsymbol{\sigma} \mathbf{I}, \quad \sigma_{\text{VM}} = \sqrt{\frac{3}{2} \boldsymbol{s} \cdot \boldsymbol{s}} \end{aligned} \quad (6.2.1)$$

Here  $\boldsymbol{\varepsilon}^{\text{pl}}$  is the creep strain tensor,  $\boldsymbol{\sigma}$  is the stress tensor,  $\omega$  is the scalar-valued damage parameter and  $\sigma_{\text{eq}}^\omega$  is the damage equivalent stress (see Sect. 5.7.1.1). The response functions  $f_1$ ,  $f_2$ ,  $g_1$ , and  $g_2$  are

$$\begin{aligned} f_1(\sigma) &= a \sigma^n, \quad g_1(\omega) = (1 - \omega)^{-n}, \\ f_2(\sigma) &= b \sigma^k, \quad g_2(\omega) = (1 - \omega)^{-k} \end{aligned} \quad (6.2.2)$$

The material parameters are presented in Liu et al. (1994) as follows

$$\begin{aligned} a &= 2.13 \cdot 10^{-13} \text{ MPa}^{-n} / \text{h}, \quad b = 9.1 \cdot 10^{-10} \text{ MPa}^{-k} / \text{h}, \\ n &= 3.5, \quad k = 2.8 \end{aligned} \quad (6.2.3)$$

Note, that the constants  $a$  and  $b$  in Eqs. (6.2.2) are identified for the constant temperature. In the general case they must be replaced by functions of temperature. It

is assumed that the damage evolution is controlled by the maximum tensile stress. Therefore the damage equivalent stress takes the form

$$\sigma_{\text{eq}}^{\omega}(\boldsymbol{\sigma}) = \frac{\sigma_I + |\sigma_I|}{2},$$

where  $\sigma_I$  is the first principal stress. The elastic material behavior is characterized by the following values of the Young's modulus  $E$  and the Poisson's ratio  $\nu$

$$E = 1.44 \cdot 10^5 \text{ MPa}, \quad \nu = 0.314 \quad (6.2.4)$$

Equations (6.2.1) can be applied for the analysis of creep under constant or proportional slowly varying loading. Response functions and material parameters in Eqs. (6.2.1) can be found in the literature for numerous metals and alloys. Examples are presented in the monographs by Boyle and Spence (1983), Lemaitre and Chaboche (1990), Malinin (1981), Penny and Marriott (1995), Podgorny et al. (1984), Rabotnov (1969), Skrzypek and Ganczarski (1998), Hyde et al. (2013). Experimental data from long-term creep tests are usually limited and the scatter is unavoidable. Therefore, robust equations (6.2.1) are widely used in modeling creep behavior and in structural analysis. Examples of material parameters as well as structural mechanics applications can be found in Altenbach et al. (1997b), Altenbach and Naumenko (1997), Altenbach et al. (2000, 2001), Bodnar and Chrzanowski (1991), Hayhurst (2001), Hyde et al. (1997, 1999, 2000), Konkin and Morachkovskij (1987), Kowalewski (1996), among others.

## 6.2.2 Steel 13CrMo4-5

In Segle et al. (1996) the creep behavior of steel 13CrMo4-5 at 550°C is described by (6.2.1) with the following response functions

$$\begin{aligned} f_1(\sigma) &= a\sigma^n, & g_1(\omega) &= 1 - \zeta + \zeta(1 - \omega)^{-n}, \\ f_2(\sigma) &= b\sigma^k, & g_2(\omega) &= (1 - \omega)^{-l} \end{aligned} \quad (6.2.5)$$

The material parameters are

$$\begin{aligned} a &= 1.94 \cdot 10^{-15} \text{ MPa}^{-n}/\text{h}, & b &= 3.302 \cdot 10^{-13} \text{ MPa}^{-k}/\text{h}, \\ n &= 4.354, & k &= 3.955, & l &= 1.423, & \zeta &= 0.393 \end{aligned} \quad (6.2.6)$$

The damage equivalent stress is assumed in the form

$$\sigma_{\text{eq}}^{\omega}(\boldsymbol{\sigma}) = \alpha \frac{\sigma_I + |\sigma_I|}{2} + (1 - \alpha)\sigma_{\text{VM}}$$

with  $\alpha = 0.43$ . The Young's modulus and Poisson's ratio are  $E = 1.6 \cdot 10^5$  MPa and  $\nu = 0.3$ , respectively. Equations (6.2.1) with response functions (6.2.5) are applied in Naumenko and Altenbach (2007) for the long-term strength analysis of a steam transfer line, see also Sect. 1.2.1.2.

### 6.2.3 Steel X20CrMoV12-1

In this section we present a set of constitutive and evolution equations to describe the inelastic behavior of advanced 9–12% Cr heat resistant steels. These materials are designed for the use at steam temperatures up to 650°C (Mayer and Masuyama 2008). If compared to the low alloy steels, they have a rather complex composition and show complicated inelastic behavior (see Chap. 1). The main features are

- The uni-axial creep curves do not exhibit a secondary (steady-state) stage. The dependence of the minimum creep rate on the stress essentially deviates from the power law (Kloc and Sklenička 2004; Kimura et al. 2009; Kostenko et al. 2009a).
- The transition from the primary to the tertiary creep stage is controlled by softening processes, e.g. the coarsening of the subgrain microstructure (Straub 1995; Polcik et al. 1998).
- The final part of the tertiary creep is influenced by damage processes, e.g. the formation and growth of voids and micro-cracks (Straub 1995; Rauch et al. 2004; Simon 2007).
- The damage and softening processes are more or less dominant for different stress ranges. As a result the slope of the creep term strength curve (stress versus time to rupture in a double logarithmic scale) continuously decreases with a decrease of the stress level (Naumenko and Kostenko 2009).
- The stress-strain curves show descending (softening) branches, Fig. 1.2.

The conventional approach in the creep continuum damage mechanics is to introduce damage parameter(s) and to calibrate the damage evolution equation(s) against the tertiary stage of the creep curve. As proposed by Rabotnov (1963) a single damage parameter can be used to describe tertiary creep and long term strength in the range of “brittle” creep rupture, see Sect. 3.6.1. On the other hand, the Hoff's kinematical model of ductile creep predicts tertiary creep as a result of the shrinkage of the specimens cross section (Hoff 1953), see Sect. 3.3. The combination of Rabotnov's and Hoff's models provides the two-slope long term strength curve including both the ductile and the brittle creep regimes (Rabotnov 1963; Odqvist 1974). Further developments of this approach were related to quantification of different damage mechanisms, e.g. creep constrained or continuum cavity nucleation and growth (Lin et al. 2005) as well as processes that accompany and influence the damage evolution, e.g. the coarsening of carbide precipitates (Dyson and McLean 2001). The resulting models include several independent internal state variables that account for different deterioration processes and characterize tertiary creep in a more precise manner (Hayhurst 1999).

Below we extend the conventional approach by quantifying hardening/recovery, softening, and damage processes. For the sake of simplicity we introduce a single damage parameter to characterize creep cavitation. The influence of ageing processes like coarsening of carbide precipitates will be ignored. We focus on the modeling of softening associated with the evolution of subgrain structure usually observed in advanced heat resistant steels. In particular, we show that a combined model including hardening, softening, and damage variables describes well the inelastic response under constant and variable loading. Furthermore, such a model allows us to reproduce the long term strength behavior in a wide stress range.

To describe hardening and softening phenomena we apply a phase mixture model discussed in Sects. 3.5.3 and 5.6.3. The response functions of stress and temperature as well as material parameters are calibrated against experimental data for X20CrMoV12-1 steel presented in Straub (1995). Creep tests under tension and compression were performed for a range of stresses and temperatures. For the compressive true stress the tertiary creep is primarily determined by the softening processes. Based on the corresponding creep curves the phase mixture model will be calibrated. For the tensile stress, additional rapid increase of the creep rate is controlled by damage evolution. This fact is confirmed by microstructural observations presented in Straub (1995), where voids and micro-cracks were detected only for tension specimen. To describe the final part of the creep curve the scalar-valued damage variable and the damage evolution equation will be utilized.

To verify the developed model, creep curves under stress changes will be simulated and the results will be compared with experimental data. To validate the coupled softening and damage evolution equations time to fracture will be simulated for different uni-axial stress levels. To discuss the applicability range of the model we simulate the inelastic behavior under strain controlled tension.

### 6.2.3.1 Hardening and Softening

The constitutive model for the inelastic deformation considering hardening/recovery and softening processes is presented in Sect. 5.6.3. The model includes the constitutive equation for the inelastic strain rate tensor (5.6.274), the evolution equation for the backstress deviator (5.6.273) and the evolution equation for the softening variable (5.6.277). For isothermal conditions the constitutive model can be formulated as follows

$$\begin{aligned}\dot{\boldsymbol{\epsilon}}^{\text{pl}} &= \frac{3}{2} f(\bar{\sigma}_{\text{vM}}) g(T) \frac{\bar{\boldsymbol{s}}}{\bar{\sigma}_{\text{vM}}} - \frac{d}{dt} \left( \frac{\boldsymbol{\beta} \Gamma}{2\mu} \right), \\ \dot{\boldsymbol{\beta}} &= \frac{2\mu}{c_h} \left( \dot{\boldsymbol{\epsilon}}^{\text{pl}} - \frac{3}{2} \dot{\boldsymbol{\epsilon}}_{\text{vM}}^{\text{pl}} \frac{\boldsymbol{\beta}}{\beta_*} \right), \\ \dot{\Gamma} &= A_s [\Gamma_*(\sigma_{\text{vM}}) - \Gamma] \dot{\boldsymbol{\epsilon}}_{\text{vM}}^{\text{pl}},\end{aligned}\tag{6.2.7}$$

where the active stress deviator  $\bar{\boldsymbol{s}}$  and the corresponding von Mises equivalent stress  $\bar{\sigma}_{\text{vM}}$  are defined as follows

$$\underline{\bar{s}} = \underline{s} - \underline{\beta} \Gamma, \quad \bar{\sigma}_{\text{VM}} = \sqrt{\frac{3}{2} \underline{\bar{s}} \cdot \underline{\bar{s}}} \quad (6.2.8)$$

The underlined term in Eq. (6.2.7)<sub>1</sub> has minor influence on the inelastic strain rates and can be neglected, as proposed in Naumenko et al. (2011a,b), Kostenko et al. (2013). For the uni-axial stress state the stress deviator  $\underline{s}$  and the backstress deviator  $\underline{\beta}$  take the following forms

$$\underline{s} = \sigma (\underline{e} \otimes \underline{e} - \frac{1}{3} \underline{I}), \quad \underline{\beta} = \beta (\underline{e} \otimes \underline{e} - \frac{1}{3} \underline{I}), \quad (6.2.9)$$

where  $\sigma$  is the uni-axial stress,  $\beta$  is the uni-axial backstress and the unit vector  $\underline{e}$  stands for the loading direction. The constitutive model (6.2.7) takes the following form

$$\begin{aligned} \dot{\varepsilon}^{\text{pl}} &= f(|\sigma - \beta \Gamma|) g(T) \frac{\sigma - \beta \Gamma}{|\sigma - \beta \Gamma|}, \\ \dot{\beta} &= \frac{3\mu}{c_h} \left( \dot{\varepsilon}^{\text{pl}} - |\dot{\varepsilon}^{\text{pl}}| \frac{\beta}{\beta_*} \right), \\ \dot{\Gamma} &= A_s [\Gamma_* (|\sigma|) - \Gamma] |\dot{\varepsilon}^{\text{pl}}| \end{aligned} \quad (6.2.10)$$

Assuming a constant stress value  $\sigma = \text{const}$  and with a new variable  $H = \beta/\sigma_0$  Eqs. (6.2.10) can be simplified as follows

$$\begin{aligned} \dot{\varepsilon}^{\text{pl}} &= f[|\sigma|(1 - H\Gamma)] g(T) \text{sgn}\sigma, \\ \dot{H} &= \frac{3\mu}{c_h \sigma} \left( 1 - \frac{H}{H_*} \right) \dot{\varepsilon}^{\text{pl}}, \quad H_* = \frac{\beta_*}{|\sigma|} \\ \dot{\Gamma} &= A_s [\Gamma_* (|\sigma|) - \Gamma] \dot{\varepsilon}^{\text{pl}} \text{sgn}\sigma \end{aligned} \quad (6.2.11)$$

With the initial condition  $H(0) = 0$  the hardening evolution equation in (6.2.11)<sub>2</sub> can be integrated leading to

$$H(\sigma, \varepsilon^{\text{pl}}) = H_* \left[ 1 - \exp \left( -\frac{3\mu}{c_h H_*} \frac{\varepsilon^{\text{pl}}}{\sigma} \right) \right] \quad (6.2.12)$$

Neglecting the softening, i.e. setting in (6.2.11)<sub>3</sub>  $A_s = 0$  and with the initial condition  $\Gamma(0) = 1$  the creep constitutive equation (6.2.11)<sub>1</sub> takes now the form

$$\dot{\varepsilon}^{\text{pl}} = f \left\{ |\sigma| \left[ 1 - H_* + H_* \exp \left( -\frac{3\mu}{c_h H_*} \frac{\varepsilon^{\text{pl}}}{\sigma} \right) \right] \right\} g(T) \text{sgn}\sigma \quad (6.2.13)$$

Equation (6.2.13) describes the primary stage of a creep curve, i.e. the decrease of the creep rate towards a steady-state value  $\dot{\varepsilon}_{\text{ss}}^{\text{pl}} = f[|\sigma|(1 - H_*)] g(T) \text{sgn}\sigma$  with an increase of the creep strain. Constitutive and evolution Eqs. (6.2.11)<sub>1</sub> and (6.2.11)<sub>2</sub> with  $\Gamma = 1$  were used in Dyson and McLean (2001), Kowalewski et al. (1994), Perrin and Hayhurst (1994) to describe primary creep of various materials, see Sects. 5.7.1.3

and 6.2.4. We observe, that Eqs. (6.2.11)<sub>1</sub> and (6.2.11)<sub>2</sub> are only applicable for the constant stress value.

For the constant stress value  $\sigma$  and with the initial condition  $\Gamma(0) = 1$  the softening evolution equation (6.2.11)<sub>3</sub> can be integrated providing the softening variable as the following function of stress and inelastic strain

$$\Gamma(\sigma, \varepsilon^{pl}) = \Gamma_*(|\sigma|) + [1 - \Gamma_*(|\sigma|)] \exp(-A_s \varepsilon^{pl} \text{sgn}\sigma) \tag{6.2.14}$$

With Eqs. (6.2.12) and (6.2.14) the inelastic strain rate (6.2.10)<sub>1</sub> is the function of the inelastic strain and the applied stress.

Figure 6.1 shows the experimental data for X20CrMoV12-1 steel at 873 K presented in Straub (1995). Creep tests were performed under constant compressive true stress. From the absolute strain values the creep rate was evaluated and plotted against the logarithmic creep strain. The resulting creep rate versus creep strain curves clearly show the hardening and softening regimes, Fig. 6.1. The experimental data is used to identify the material parameters and response functions in Eqs. (6.2.10)<sub>1</sub>, (6.2.12) and (6.2.14). To calibrate a constitutive model a family of creep curves in wide stress and temperature ranges is usually required. Creep curves presented in Fig. 6.1 are given for one temperature level and for a narrow stress range. Therefore additional experimental data on minimum creep rates is applied for the identification. Figure 6.1 shows the minimum creep rate as a function of stress for three temperature levels. The experimental data is collected by Straub (1995) from several publications and based on own creep tests. To fit the data various response functions of stress and temperature, which are more or less physically motivated, can be applied. Overviews are presented in Sect. 5.4.4. One example is the hyperbolic sine law

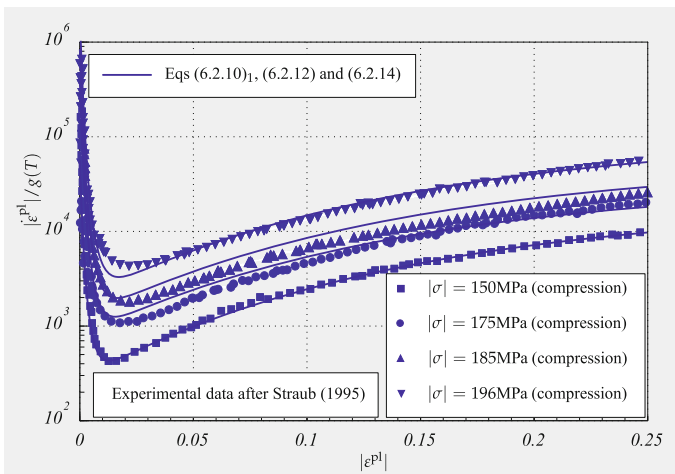


**Fig. 6.1** Normalized creep rate versus creep strain curves for X20CrMoV12-1 steel at 873 K and different stress levels

$$\dot{\epsilon}_{\min} = g(T) \sinh(B\sigma), \tag{6.2.15}$$

where  $B$  is a constant and  $g(T)$  is the Arrhenius function of the absolute temperature  $T$ . Equation (6.2.15) is applied in Dyson and McLean (2001), Kowalewski et al. (1994), Perrin and Hayhurst (1994). Another way is to assume that the minimum creep rate is the sum of the linear and the power law stress functions. As pointed out in Frost and Ashby (1982) power law and diffusion creep mechanisms involve different defects and may be assumed independent such that the corresponding creep rates add. The constitutive equation can be formulated as follows

$$\dot{\epsilon}_{\min} = \dot{\epsilon}_0(T) \frac{\sigma}{\sigma_0(T)} + \dot{\epsilon}_0(T) \left( \frac{\sigma}{\sigma_0(T)} \right)^n, \tag{6.2.16}$$

where  $n$  is a constant and  $\dot{\epsilon}_0(T)$ ,  $\sigma_0(T)$  are Arrhenius functions of the temperature. The response function (6.2.16) is applied in Kloc and Sklenička (2004), Rieth et al. (2004), Naumenko and Kostenko (2009), Naumenko et al. (2009) to describe the minimum creep rate for various advanced steels. The results of fitting by the use of Eqs. (6.2.15) and (6.2.16) are presented in Fig. 6.2. In what follows let us apply the hyperbolic sine law. The identified response functions in Eqs. (6.2.10) can be summarized as follows

$$\begin{aligned} f(x) &= \sinh(Bx), & g(T) &= a_0 \exp\left(-\frac{\alpha}{T}\right), \\ \Gamma_*(x) &= \frac{a_\Gamma}{1 + b_\Gamma e^{-\frac{x}{c_\Gamma}}}, & \beta_*(x) &= H_* x \end{aligned} \tag{6.2.17}$$

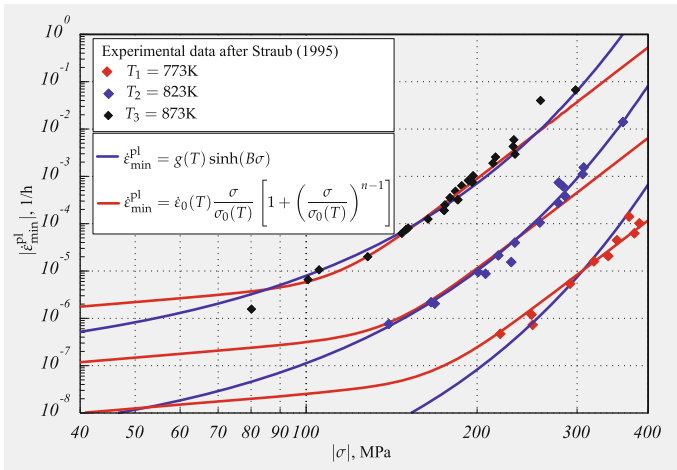


**Fig. 6.2** Minimum creep rate versus stress curves for X20CrMoV12-1 steel at three temperature levels

with  $B = 7.74 \cdot 10^{-2}$  1/MPa,  $a_0 = 4.64 \cdot 10^{23}$  1/h,  $\alpha = 6.12 \cdot 10^4$  1/K,  $a_\Gamma = 0.42$ ,  $b_\Gamma = 9.12 \cdot 10^6$ ,  $c_\Gamma = 9.46$  MPa,  $H_* = 0.46$ . The additional material parameters in Eqs. (6.2.10) are identified as  $c_h = 8.84$  and  $A_s = 7.21$ . The Young's modulus  $E$  and the shear modulus  $\mu$  are functions of temperature. The corresponding temperature dependencies are given in Straub (1995) as follows

$$E(T) = -a_E + b_E T, \quad \mu(T) = -a_\mu + b_\mu T \quad (6.2.18)$$

with

$$\begin{aligned} a_E &= 95.597 \text{ MPa/K}, & b_E &= 252334.26 \text{ MPa}, \\ a_\mu &= 38.773 \text{ MPa/K}, & b_\mu &= 97398.16 \text{ MPa} \end{aligned}$$

### 6.2.3.2 Damage Processes and Creep Strength

Damage processes are usually associated with nucleation, growth and coalescence of voids on grain or subgrain boundaries as well as nucleation of voids and microcracks around carbide precipitates. For low-alloy steels the damage evolution equations are usually calibrated against the tertiary stage of the creep curve. For advanced steels the essential part of the tertiary creep is related to softening processes (e.g. coarsening of subgrain structure) as documented in Polcik et al. (1999), Kimura (2006), Kostenko and Naumenko (2008), see also Fig. 1.9. For 9%Cr steels the voids on former austenite grain boundaries and/or carbides can be observed after prolonged test durations and essentially higher values of the creep strain if compared to the low alloy steels, e.g. Rauch et al. (2004), Maile and Scheck (2008). Let us describe the uni-axial creep curves for X20CrMoV12-1 steel presented in Straub (1995). To this end we introduce the Kachanov-Rabotnov damage parameter (Rabotnov 1963) and apply the strain equivalence principle as proposed in Lemaitre and Chaboche (1990), see Sects. 3.6.1 and 5.7.1.1. The constitutive equation (6.2.10)<sub>1</sub> can be modified as follows

$$\dot{\varepsilon}^{\text{pl}} = f \left( \frac{|\sigma - \beta \Gamma|}{1 - \omega} \right) \frac{\sigma - \beta \Gamma}{|\sigma - \beta \Gamma|} \quad (6.2.19)$$

For the damage parameter  $\omega$  the evolution (3.6.135) equation is applied

$$\dot{\omega} = h_\omega(\omega) \frac{1 + \text{sgn}\sigma}{2} \frac{|\dot{\varepsilon}^{\text{pl}}|}{\varepsilon_*^{\text{pl}}(|\sigma|)}, \quad (6.2.20)$$

where  $h_\omega(\omega)$  and  $\varepsilon_*^{\text{pl}}(|\sigma|)$  are response functions. Figure 6.3 shows creep curves for X20CrMoV12-1 steel obtained from tension tests under constant true stress levels. For the comparison the creep curves under compression for the same stress levels are presented. The results of metallographic analysis presented in Straub (1995) show that the increase in the creep rate under tension is primarily connected with the nucleation and growth of voids. Therefore the continuum damage mechanics can be applied to describe the whole creep process including the final part before the

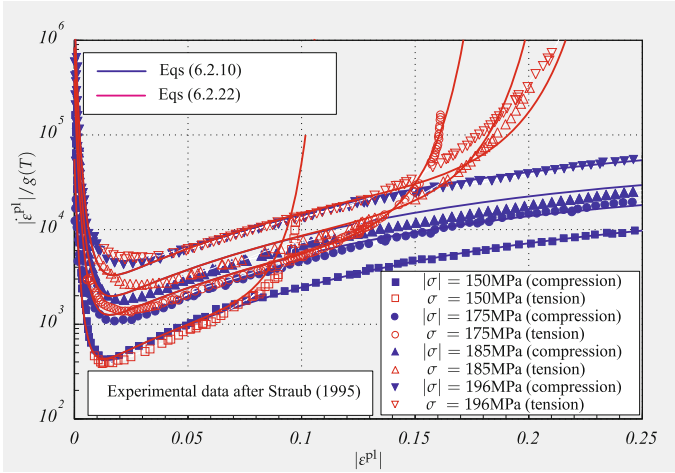


**Fig. 6.3** Normalized creep rate versus creep strain curves for X20CrMoV12-1 steel at 873 K and different stress levels

fracture. Let us summarize all constitutive and evolution equations for the uni-axial stress state as follows

$$\begin{aligned}
 \dot{\varepsilon}^{pl} &= f(|\sigma - \beta\Gamma|)g(T) \frac{\sigma - \beta\Gamma}{|\sigma - \beta\Gamma|}, \\
 \dot{\beta} &= \frac{3\mu}{c_h} \left( \dot{\varepsilon}^{pl} - |\dot{\varepsilon}^{pl}| \frac{\beta}{\beta_*} \right), \\
 \dot{r} &= A_s [\Gamma_*(|\sigma|) - \Gamma] |\dot{\varepsilon}^{pl}|, \\
 \dot{\omega} &= h_\omega(\omega) \frac{1 + \text{sgn}\sigma}{2} \frac{|\dot{\varepsilon}^{pl}|}{\varepsilon_*^{pl}(|\sigma|)},
 \end{aligned} \tag{6.2.21}$$

The response functions in the damage evolution equation are identified as follows

$$h_\omega(\omega) = l\omega^{\frac{l-1}{l}}, \quad \varepsilon_*^{pl}(|\sigma|) = \varepsilon_{br} + \frac{a_\varepsilon}{1 + b_\varepsilon \exp\left(-\frac{|\sigma|}{c_\varepsilon}\right)} \tag{6.2.22}$$

with  $l = 8$ ,  $\varepsilon_{br} = 0.09$ ,  $a_\varepsilon = 0.2$ ,  $b_\varepsilon = 8.39 \cdot 10^5$ ,  $c_\varepsilon = 12.67$  MPa.

Numerical integration of Eqs. (6.2.21) over time provides the relation between the applied stress and the time to rupture. Figure 6.4 shows the results of integration according to three different model assumptions. The model of ductile creep rupture proposed by Hoff (1953) ignores softening and damage processes. The tertiary creep stage is the result of the specimens cross section shrinkage only, see Sect. 3.4. This approach provides a rough estimation of the time to creep rupture, Fig. 6.4. If softening processes are taken into account then the long term strength curve shifts

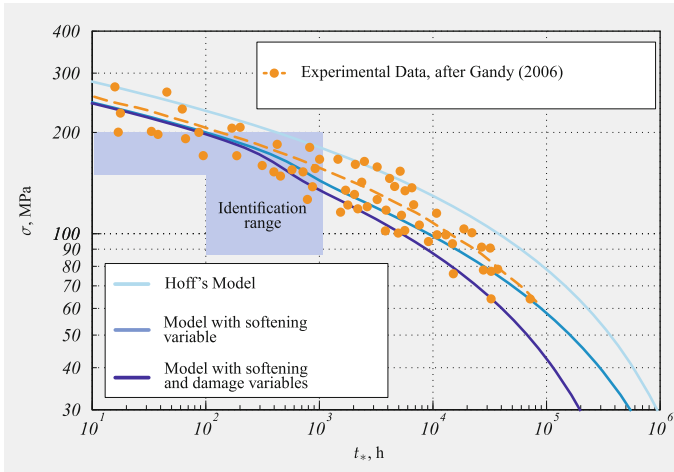


**Fig. 6.4** Engineering stress versus time to rupture for X20CrMoV12-1 steel at 873 K

down along the stress axis. Furthermore, a sigmoidal inflection of the creep strength curve can be observed, Fig. 6.4. Such sigmoidal inflection is documented in many experimental studies related to advanced 9–12 % Cr steels (Abe 2004; Kimura et al. 1997; Sklenička et al. 2003).

If we consider both the softening and the damage processes an additional decrease of the slope of the long term strength curve can be described. Let us note that hardening, softening and damage evolution equations are calibrated against the creep curves in a narrow stress range (identification range). To check the quality of lifetime prediction in the wide stress range let us compare the results with experimental data plotted by dots in Fig. 6.4 after Gandy (2006). Despite a relatively large scatter of the data, we may conclude that the Hoff's model overestimates the rupture life in the range of moderate and low stress levels. The softening model leads to the result closer to experimental data while the additional consideration of damage provides a conservative estimation of the lifetime.

Voids and microcracks usually nucleate and grow on those planes which are perpendicular to the direction of the maximum tensile stress, e.g. Naumenko and Altenbach (2007), Betten (2008). The microstructural observations and the analysis of void size distributions in crept specimen from steels X20CrMoV12-1 and X22CrMoV12-1 are presented in Straub (1995). The biggest voids were found within the angles  $60^\circ$ – $90^\circ$  to the stress axis. The topology of the directional damage state can be characterized by damage tensors of different rank, see Sect. 5.7.2. To establish the influence of the directional damage on the creep rate, creep tests under non-proportional loading conditions are required. Examples include creep tests on thin-walled tubes under combined tension and torsion (Murakami and Sanomura 1985) and biaxial creep tests on cruciform specimens (Sakane and Tokura 2002). The results of such tests can be applied to calibrate the tensor-valued damage evolu-

tion equations. Multi-axial test data for 9–12% Cr steels are currently not published. Here we neglect the directional nature of damage. The damage evolution equation (6.2.20) can be generalized as follows

$$\dot{\omega} = h_{\omega}(\omega) \frac{1}{2} \frac{(\sigma_I + |\sigma_I|)}{\sigma_{vM}} \frac{\dot{\epsilon}_{vM}^{pl}}{\epsilon_*^{pl}(\sigma_{vM})}, \tag{6.2.23}$$

where  $\sigma_I$  is the first principal stress. Applying the strain equivalence principle (Lemaitre and Chaboche 1990; Lemaitre 1996) the constitutive equation (6.2.7)<sub>1</sub> can be generalized as follows

$$\dot{\epsilon}^{pl} = \frac{3}{2} f \left( \frac{\bar{\sigma}_{vM}}{1 - \omega} \right) g(T) \frac{\bar{s}}{\bar{\sigma}_{vM}} \tag{6.2.24}$$

### 6.2.3.3 Creep Under Stress Changes

To verify the constitutive model let us simulate creep behavior under variable loading conditions. Figure 6.5 shows the experimental creep curve under compressive stress changes obtained in Straub (1995). During the test the specimen was initially subjected to the constant compressive true stress with the value of 196 MPa. After a certain hold time the stress was rapidly reduced to the value of 150 MPa. Several loading/unloading cycles with hold time were performed up to the reaching of the creep strain value of 25%. As Fig. 6.5 shows the stress changes were performed within the tertiary creep stage.

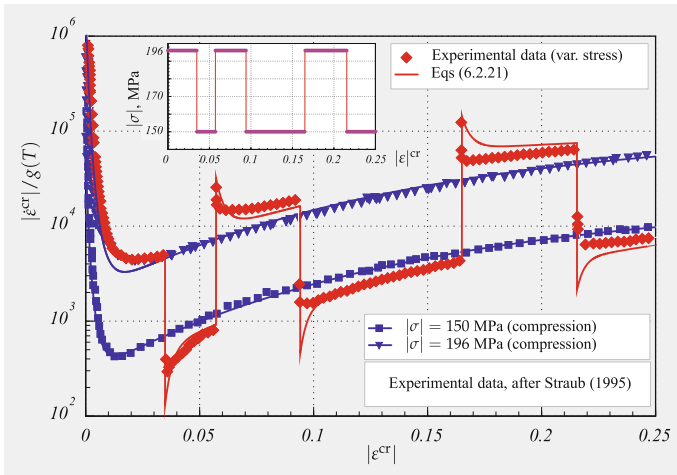


**Fig. 6.5** Normalized creep rate versus creep strain for X20CrMoV 12-1 steel at  $T = 600\text{ }^{\circ}\text{C}$  and variable compressive stress

The inelastic strain rate versus inelastic strain curve predicted by Eqs. (6.2.21) is presented in Fig. 6.5 by the solid line. For the comparison, two creep curves under the constant upper and lower stress values are shown. We observe that the model underestimates the creep rates after the rapid loading reduction. This slight disagreement may be related to the deficiency of the assumed constitutive equation for the inelastic-hard constituent in the phase mixture model, see Sect. 5.6.3. Despite this inaccuracy, the creep behavior under stress changes is well represented by the composite model with the varying volume fraction. One feature of the softening process is well reproduced by the model. After the stress decrease the creep rate remains lower, while after the stress increase remains higher than the corresponding creep rates under the constant stress levels.

#### 6.2.3.4 Tensile Behavior Under Constant Strain Rate

The next verification test is to simulate tensile behavior under a constant strain rate. To compute the stress response we integrate the equation

$$\dot{\varepsilon} = \frac{\dot{\sigma}}{E} + \dot{\varepsilon}^{\text{pl}} = \text{const} \quad (6.2.25)$$

together with the constitutive model (6.2.21). Figure 6.6 shows the experimental stress-strain diagram obtained with  $\dot{\varepsilon} = 2.63 \cdot 10^{-4} \text{ s}^{-1}$  and 803 K (Röttger 1997). The results of the model prediction are presented by the solid line. In addition, a zoom of the transition from the linear-elastic to the inelastic behavior is given in the left smaller diagram. The right smaller diagram shows the backstress variable  $\beta$  as a function of the strain. The elastic behavior up to 300 MPa is almost exactly described. The beginning of the inelastic behavior is observed at the strain value  $\varepsilon \approx 0.0015$ . Up to this value the backstress remains almost zero. It is obvious that there is no kink in the progress of the global stress-strain curve, although the change of the slope is too abrupt if compared to the experimental data. The too strict transition from the linear-elastic to the inelastic behavior and a low slope of the curve at the beginning of the inelastic range may again be related to the deficiency of the assumed constitutive equation for the inelastic-hard constituent in the phase mixture model, see Sect. 5.6.3. Nevertheless, the maximum stress value and the softening behavior are well reproduced by the model. For strains higher than 16 % the model overestimates the stress values. This may be caused by the start of necking of the specimen, which is not taken into account in the uni-axial model.

#### 6.2.3.5 Summary of Constitutive and Evolution Equations

The proposed constitutive model includes three state variables: the backstress deviator  $\beta$ , the softening variable  $\Gamma$  and the damage variable  $\omega$ . The inelastic strain tensor and the internal state variables are defined by the following equations

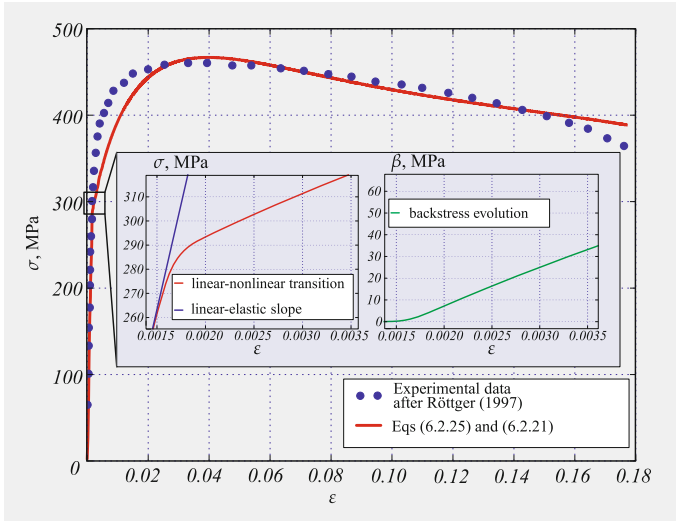


**Fig. 6.6** Stress-strain diagram for X20CrMoV12-1 steel with  $\dot{\epsilon} = 2.63 \cdot 10^{-4} \text{ s}^{-1}$  at 803 K

$$\begin{aligned}
 \dot{\epsilon}^{\text{pl}} &= \frac{3}{2} f \left( \frac{\bar{\sigma}_{\text{vM}}}{1 - \omega} \right) g(T) \frac{\bar{\mathbf{s}}}{\bar{\sigma}_{\text{vM}}}, \\
 \dot{\boldsymbol{\beta}} &= \frac{2\mu}{c_h} \left[ \dot{\epsilon}^{\text{pl}} - \frac{3}{2} \dot{\epsilon}_{\text{vM}}^{\text{pl}} \frac{\boldsymbol{\beta}}{\beta_*(\sigma_{\text{vM}})} \right], \\
 \dot{\Gamma} &= A_s [\Gamma_*(\sigma_{\text{vM}}) - \Gamma] \dot{\epsilon}_{\text{vM}}^{\text{pl}}, \\
 \dot{\omega} &= h_\omega(\omega) \frac{1}{2} \frac{(\sigma_I + |\sigma_I|)}{\sigma_{\text{vM}}} \frac{\dot{\epsilon}_{\text{vM}}^{\text{pl}}}{\epsilon_*^{\text{pl}}(\sigma_{\text{vM}})}
 \end{aligned} \tag{6.2.26}$$

with the active stress deviator  $\bar{\mathbf{s}}$  and the corresponding von Mises equivalent stress  $\bar{\sigma}_{\text{vM}}$

$$\bar{\mathbf{s}} = \mathbf{s} - \boldsymbol{\beta} \Gamma, \quad \bar{\sigma}_{\text{vM}} = \sqrt{\frac{3}{2} \bar{\mathbf{s}} \cdot \bar{\mathbf{s}}} \tag{6.2.27}$$

The response functions  $f$ ,  $g$ ,  $\beta_*$ ,  $\Gamma_*$ ,  $h_\omega$  and  $\epsilon_*^{\text{pl}}$  and the material parameters  $c_h$ ,  $A_s$  must be identified from families of creep and tensile curves for a range of stresses, temperatures and strain rates. For 12%Cr steel X20CrMoV12-1 these functions are calibrated from experimental data on creep as follows

$$\begin{aligned}
 f(x) &= \sinh(Bx), \quad g(T) = a_0 \exp\left(-\frac{\alpha}{T}\right), \\
 \Gamma_*(x) &= \frac{a_\Gamma}{1 + b_\Gamma \exp\left(-\frac{x}{c_\Gamma}\right)}, \quad \beta_*(x) = H_* x, \\
 h_\omega(\omega) &= l\omega^{\frac{l-1}{l}}, \quad \varepsilon_*^{\text{pl}}(|\sigma|) = \varepsilon_{br} + \frac{a_\varepsilon}{1 + b_\varepsilon \exp\left(-\frac{|\sigma|}{c_\varepsilon}\right)}
 \end{aligned} \tag{6.2.28}$$

with the material parameters

$$\begin{aligned}
 B &= 7.74 \cdot 10^{-2} \text{ 1/MPa}, \quad a_0 = 4.64 \cdot 10^{23} \text{ 1/h}, \quad \alpha = 6.12 \cdot 10^4 \text{ 1/K}, \\
 c_h &= 8.84, \quad H_* = 0.46, \\
 A_s &= 7.21, \quad a_\Gamma = 0.42, \quad b_\Gamma = 9.12 \cdot 10^6, \quad c_\Gamma = 9.46 \text{ MPa}
 \end{aligned} \tag{6.2.29}$$

The Young's modulus  $E$  and the shear modulus  $\mu$  are identified in Straub (1995) as follows

$$E(T) = -a_E + b_E T, \quad \mu(T) = -a_\mu + b_\mu T \tag{6.2.30}$$

with

$$\begin{aligned}
 a_E &= 95.597 \text{ MPa/K}, \quad b_E = 252334.26 \text{ MPa}, \\
 a_\mu &= 38.773 \text{ MPa/K}, \quad b_\mu = 97398.16 \text{ MPa}
 \end{aligned}$$

In a slightly modified form Eqs. (6.2.26) are applied in Kostenko and Naumenko (2008), Kostenko et al. (2009a, b), Naumenko et al. (2011b), Kostenko et al. (2013) to describe inelastic behavior of 10%Cr steels.

The advantage of the phase mixture model is the possibility to describe the inelastic behavior with a minimum number of response functions and material parameters. The developed model is compatible with the standard structural mechanics and can be implemented inside any finite element code. Since the model incorporates both the softening and damage variables and reproduces the descending branch of the stress-strain curve, regularization techniques (de Borst 2004) might be necessary to avoid spurious mesh dependence.

To improve the model, in particular for the better description of inelastic transients under rapid loading changes, the constitutive equation for the inelastic hard constituent should be refined. Another possibility is to consider a phase mixture with three or more constituents. This would lead to several backstress variables and increase the number of material parameters.

### 6.2.4 Aluminium Alloy BS 1472

The experimental data for aluminium alloy BS 1472 at  $150 \pm 0.5^\circ\text{C}$  (Al, Cu, Fe, Ni, Mg and Si alloy) are published in Kowalewski et al. (1994). The authors proposed to describe the uni-axial creep curves (loading conditions 227.53, 241.3 and 262 MPa) by use of two constitutive models. The first model is based on Eqs. (6.2.1) and the time hardening function

$$\dot{\boldsymbol{\varepsilon}}^{\text{pl}} = \frac{3}{2} \frac{a\sigma_{\text{vM}}^{n-1}}{(1-\omega)^n} \boldsymbol{s} t^m, \quad \dot{\omega} = \frac{b(\sigma_{\text{eq}}^\omega)^k}{(1-\omega)^l} t^m \quad (6.2.31)$$

with  $\sigma_{\text{eq}}^\omega = \sigma_{\text{vM}}$ . The material parameters in Eqs. (6.2.31) are identified as follows (Kowalewski et al. 1994)

$$\begin{aligned} a &= 3.511 \cdot 10^{-31} \text{ MPa}^{-n}/\text{h}^{m+1}, & b &= 1.960 \cdot 10^{-23} \text{ MPa}^{-k}/\text{h}^{m+1}, \\ n &= 11.034, & k &= 8.220, & l &= 12.107, & m &= -0.3099 \end{aligned} \quad (6.2.32)$$

The Young's modulus and Poisson's ratio are  $E = 0.71 \cdot 10^5$  MPa and  $\nu = 0.3$ . Equations (6.2.31) include the time hardening function. One shortcoming of the time hardening model is that the creep behavior depends on the choice of the time scale (see Sect. 5.6.1).

Alternatively the experimental data presented in Kowalewski et al. (1994) can be described by the following equations

$$\dot{\boldsymbol{\varepsilon}}^{\text{pl}} = \frac{3}{2} \frac{a\sigma_{\text{vM}}^{n-1}}{(1-\omega)^m} \boldsymbol{s}, \quad \dot{\omega} = \frac{b(\sigma_{\text{eq}}^\omega)^k}{(1-\omega)^l} \quad (6.2.33)$$

with the following set of material parameters

$$\begin{aligned} a &= 1.35 \cdot 10^{-39} \text{ MPa}^{-n}/\text{h}, & b &= 3.029 \cdot 10^{-35} \text{ MPa}^{-k}/\text{h}, \\ n &= 14.37, & k &= 12.895, & l &= 12.5, & m &= 10 \end{aligned} \quad (6.2.34)$$

In the above equations the primary creep effect is neglected. Figure 6.7 presents the experimental results and the predictions by Eqs. (6.2.31) and (6.2.33).

The second approach applied in Kowalewski et al. (1994) is based on the mechanism-based model (see Sect. 5.7.1.3). The constitutive model can be summarized as follows

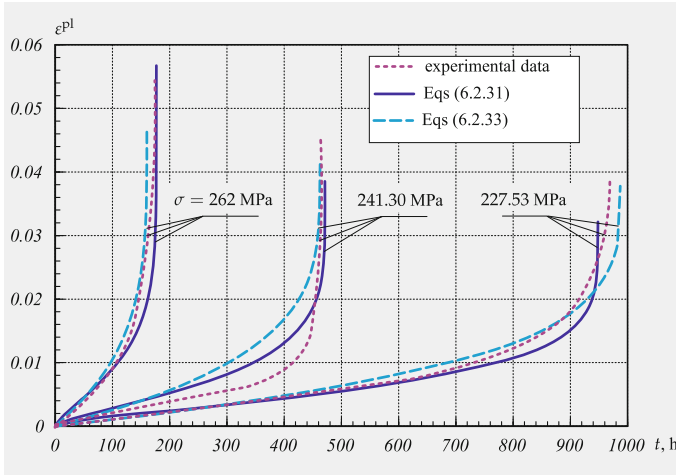


**Fig. 6.7** Experimental data and model predictions for the aluminium alloy BS 1472 at  $150 \pm 0.5^\circ\text{C}$ , after Kowalewski et al. (1994)

$$\begin{aligned}
 \dot{\varepsilon}^{\text{pl}} &= \frac{3}{2} \frac{A}{(1-\omega)^n} \frac{s}{\sigma_{\text{VM}}} \sinh \left[ \frac{B\sigma_{\text{VM}}(1-H)}{1-\Phi} \right], \\
 \dot{H} &= \frac{h_c}{\sigma_{\text{VM}}} \frac{A}{(1-\omega)^n} \sinh \left[ \frac{B\sigma_{\text{VM}}(1-H)}{1-\Phi} \right] \left( 1 - \frac{H}{H_*} \right), \\
 \dot{\Phi} &= \frac{K_c}{3} (1-\Phi)^4, \\
 \dot{\omega} &= \frac{DA}{(1-\omega)^n} \left( \frac{\sigma_I}{\sigma_{\text{VM}}} \right)^v N \sinh \left[ \frac{B\sigma_{\text{VM}}(1-H)}{1-\Phi} \right], \\
 n &= \frac{B\sigma_{\text{VM}}(1-H)}{1-\Phi} \coth \left[ \frac{B\sigma_{\text{VM}}(1-H)}{1-\Phi} \right], \\
 N &= 1 \text{ for } \sigma_I > 0, \quad N = 0 \text{ for } \sigma_I \leq 0, \\
 0 &\leq \omega < 0.3, \quad 0 \leq \Phi < 1, \quad 0 \leq H \leq H_*
 \end{aligned} \tag{6.2.35}$$

The set of equations (6.2.35) includes the creep constitutive equation and evolution equations with respect to three internal state variables. The hardening variable  $H$  is introduced to describe primary creep. The variable  $\Phi$  characterizes the ageing process. The variable  $\omega$  is responsible for the grain boundary creep constrained cavitation.

The material parameters in Eqs. (6.2.35) may be divided into three groups: the constants  $h_c$  and  $H_*$  must be obtained from the primary creep stage;  $A$  and  $B$  characterize the secondary creep (minimum creep rate versus stress); and  $K_c$  and  $D$  must be found from the tertiary creep stage. The parameter  $v$  is the so-called stress state index, which characterizes the stress state dependence of the damage evolution. The material constants are identified in Kowalewski et al. (1994) as follows

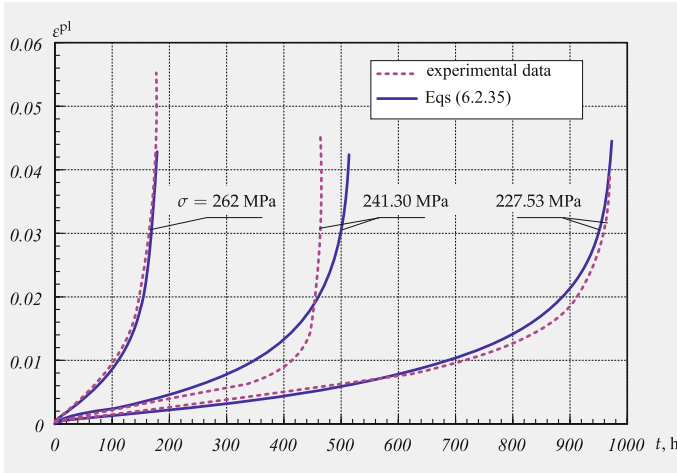


**Fig. 6.8** Experimental data and simulations for the aluminium alloy BS 1472 at  $150 \pm 0.5^\circ\text{C}$ , after Kowalewski et al. (1994)

$$\begin{aligned}
 A &= 2.960 \cdot 10^{-11} \text{ h}^{-1}, & B &= 7.167 \cdot 10^{-2} \text{ MPa}^{-1}, \\
 h_c &= 1.370 \cdot 10^5 \text{ MPa}, & H_* &= 0.2032, \\
 K_c &= 19.310 \cdot 10^{-5} \text{ h}^{-1}, & D &= 6.630
 \end{aligned}
 \tag{6.2.36}$$

Figure 6.8 presents the experimental creep curves and predictions based on Eqs. (6.2.35). To identify the stress state index  $\nu$  experimental data from multi-axial creep tests up to creep rupture are required. The isochronous rupture loci obtained according to Eqs. (6.2.35) for different values of  $\nu$  in the range  $0 \leq \nu \leq 12$  are presented in Kowalewski et al. (1994).

This example illustrates that the same experimental data can be described by different relations (6.2.31), (6.2.33) and (6.2.35). The model (6.2.35) seems to be more preferable since it is based on material science foundations. One feature of Eqs. (6.2.35) is the use of a hyperbolic function for the dependence of the minimum creep rate on the stress instead of the power function in Eqs. (6.2.33). Let us compare how the models (6.2.33) and (6.2.35) describe the secondary creep rate for a wide stress range. For this purpose we assume  $\omega \ll 1$  in Eqs. (6.2.33) leading to the Norton-Bailey creep equation  $\dot{\epsilon}_{\min}^{\text{cr}} = a\sigma^n$ . In Eq. (6.2.35) we set  $H = H_*$ ,  $\omega \ll 1$  and  $\Phi \ll 1$  resulting in  $\dot{\epsilon}_{\min}^{\text{cr}} = A \sinh[B\sigma(1 - H_*)]$ . Figure 6.9 shows the minimum creep rate as a function of stress calculated by the use of material parameters (6.2.34) and (6.2.36). We observe that within the stress range 227–262 MPa the minimum creep rate versus stress curves almost coincide. The coincidence of curves is not surprising since the material parameters in both models were identified from creep tests carried out within the stress range 227–262 MPa. This stress range is marked in Fig. 6.9 as the identification range. Furthermore, a wider stress range exist, for which the power law and the hyperbolic sine functions provide nearly the same

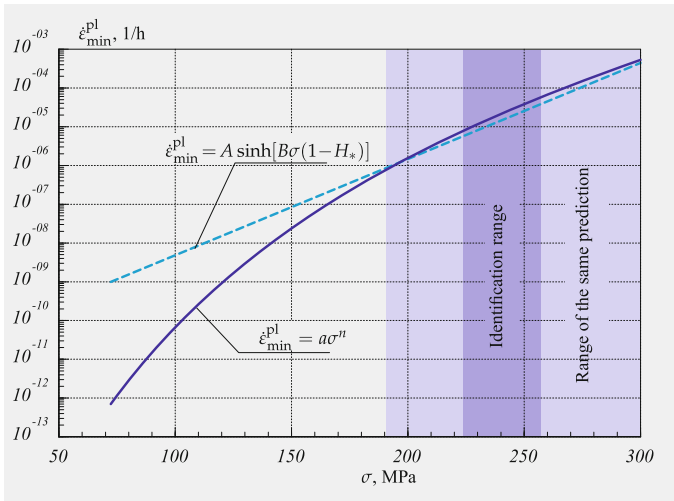


**Fig. 6.9** Minimum creep rate versus stress by use of the power law and sinh functions

inelastic strain rates, Fig. 6.9. If a structure is loaded in such a way that the von Mises equivalent stress lies within this range, then both the models would lead to similar results of structural analysis, e.g. time dependent deformation, stress redistribution etc.

However, in most applications one has to analyze statically indeterminate structures. In this case, if the external loads are constant, the stresses may rapidly relax down at the beginning of the creep process. Therefore, the range of moderate and small stress values is important in the structural analysis. For this range the two applied models lead to quite different predictions, Fig. 6.9. In Altenbach et al. (1997a, c) we utilized the models (6.2.33) and (6.2.35) for the structural analysis of pressurized cylindrical shells and transversely loaded rectangular plates. The maximum values of the von Mises equivalent stress in the reference elastic state of structures were within the identification range. The results of creep analysis based on the models (6.2.33) and (6.2.35) qualitatively agree only at the beginning of the creep process as long as the maximum values of the von Mises equivalent stress lay within the range of the same prediction. With the relaxation and redistribution of stresses, the discrepancy between the results increases leading to quite different long term predictions. The differences in estimated life times were of up to a factor 5.

### 6.3 Initially Anisotropic Materials

Many materials exhibit anisotropic inelastic behavior as a result of processing. This Section presents examples of constitutive equations for initially-anisotropic materi-

als. The first one is related to the forged aluminium alloy AA2014. Microstructural observations and experimental data suggest that the anisotropy of inelastic behavior is primarily caused by elongated grains and grain boundaries as a result of material processing. The second example deals with a multi-pass weld metal. Here the arrangement of weld beads and microstructural zones is the reason for anisotropic creep.

### 6.3.1 Forged Al-Cu-Mg-Si Alloy

Age-hardenable alloys based on the aluminum-copper system (known as AA2xxx alloys) exhibit superior creep strength and are widely used in structural components operating at elevated temperatures (Polmear 1996, 2004). Complex shape parts produced from these alloys usually exhibit microstructural anisotropy as a result of processing (Gariboldi and Conte 2013). Furthermore, the creep properties of age-hardenable alloys strongly depend on the heat treatment and ageing conditions (Gariboldi and Casaro 2007). Origins of anisotropic creep include elongated grains, crystallographic texture, non-uniform distribution of particles, oriented grain boundary cavities, etc. One approach to formulate a constitutive equation for anisotropic creep is based on the theory of symmetries and representation of tensor-valued functions, see Sect. 5.4.3. For the assumed symmetry class, e.g. a transverse isotropy, a creep potential is formulated as a function of appropriate invariants of the stress tensor. The resulting creep constitutive equation includes a number of material parameters to be identified from experimental creep curves for different stress states and different loading directions. This approach provides a general form of a constitutive equation. However, the identification of all required parameters is usually not feasible since the required experimental creep curves are rarely available.

#### 6.3.1.1 Basic Features of Microstructure

Al-Cu-Mg-Si alloy forging had displayed anisotropic effects in longitudinal (L), transverse (T) and radial (R) sampling directions (Gariboldi et al. 2016). Two sets of  $20 \times 20 \times 100 \text{ mm}^3$  bars were sampled from the as supplied forging with their longer side in L, T and R directions, respectively. Tensile tests were performed at temperatures within the range 20–170 °C. Creep tests were conducted under constant load at 130, 150 and 170 °C (homologous temperature range 0.44–0.49) under stresses that led to a range of times to rupture  $t_*$  from several hours to more than 10,000 h. Crept specimens were diametrically cut in order to investigate microstructure features along the gauge length.

The investigated forging was characterized by grains elongated in the main plastic flow path experienced during the processing. Their mean size of grains was about 300, 80 and 50  $\mu\text{m}$  along the L, T and R directions, respectively. Figure 6.10 shows light optical microscope micrographs of the microstructure of the forged part in

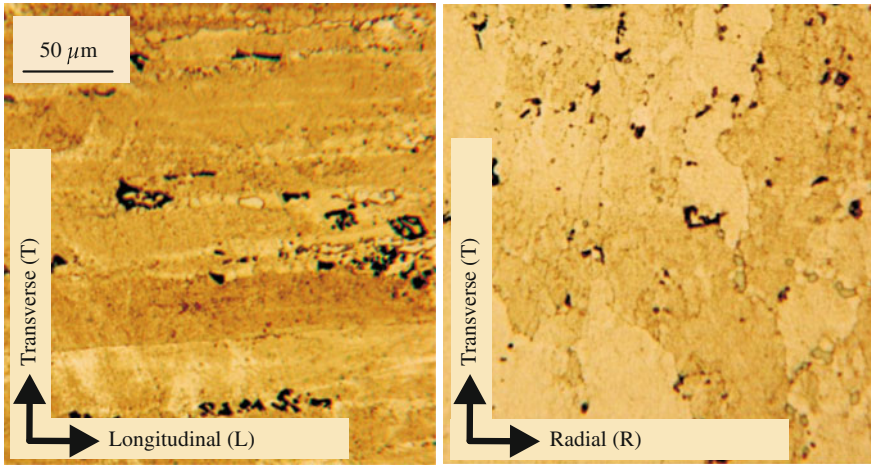


**Fig. 6.10** Light optical microscope micrographs of the forged part from AA2014 in different metallographic sections, after Gariboldi et al. (2016)

2014 alloy in different metallographic sections. Two kinds of coarse intermetallic particles were present in the microstructure: globular  $\text{Al}_2\text{Cu}$  ( $\theta$ ) particles (bright particles in Fig. 6.10) and blocky shaped clustered particles containing Fe, Mn, Si and Cu (darker particles in Fig. 6.10). These latter secondary phase clustered particles are elongated in the L direction. In most of the volume of the forging, macrographic analyzes revealed the large intermetallic particles longitudinally oriented, suggesting the same direction of the plastic flow during the processing.

In addition, transmission electron microscopy images published in Angella et al. (2008) illustrate the presence of  $\theta'$  phase, in the form of plate-like precipitates in  $\{100\}$  crystallographic planes of the  $\alpha$ -Al matrix. These precipitates play an important role in strengthening of the alloy. The forging was supplied in the T6 condition, that is the solution treatment at 778 K and aging at 433 K for 16h. During the subsequent creep overageing processes take place leading to the increase of particles size and distance between particles with time.

### 6.3.1.2 Minimum Creep Rates

Creep curves of the material sampled in L and T direction are presented and analyzed in Naumenko and Gariboldi (2014). Figure 6.11 shows minimum creep rate vs stress curves. To normalize the data the reference stress  $\sigma_0 = 320$  MPa, the reference strain rate  $\dot{\epsilon}_0 = 1.026$  1/h and the Arrhenius function of the temperature

$$g(T) = \exp\left(-\frac{Q}{RT}\right) \quad (6.3.37)$$

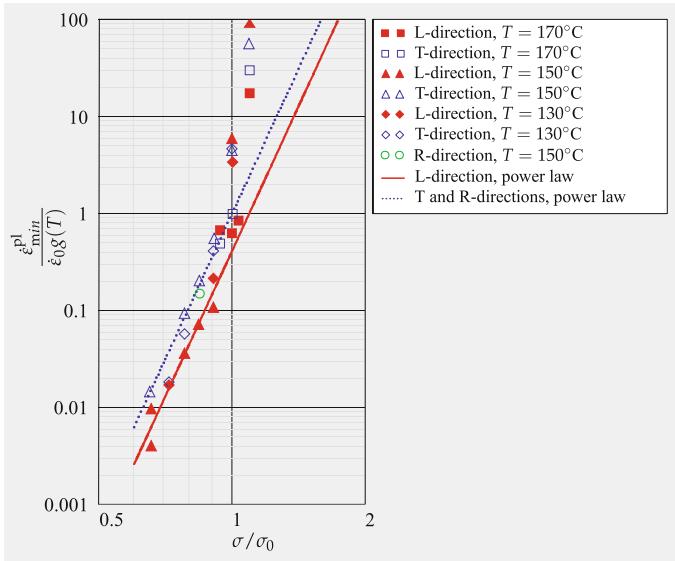


**Fig. 6.11** Normalized minimum creep rate versus normalized stress for longitudinal, transverse and radial creep tests of AA2014 at 150 °C, after Gariboldi et al. (2016)

with apparent activation energy  $Q$ , the universal gas constant  $R$  and absolute temperature  $T$  is applied. The value  $Q = 175.42$  kJ/mol is used as given in Gariboldi and Casaro (2007), Naumenko and Gariboldi (2014). The reference stress  $\sigma_0$  is introduced to split the ranges of power law creep and power law breakdown, as shown in Fig. 6.11. According to experimental data presented in Fig. 6.11 the anisotropy is primarily observable in the power law range. The following relation

$$\dot{\epsilon}_{T_{\min}}^{pl} = \alpha \dot{\epsilon}_{L_{\min}}^{pl}, \quad \alpha = 2.43$$

indicates that the creep rate in the T direction is 2.43 times higher than the creep rate in the L direction for the same stress level. In the power law breakdown range the difference between L and T data is not significant, if compared to the usual scatter of experimental data in the creep range, and can be neglected. The minimum creep rates for T-specimen can be described by the following equation

$$\dot{\epsilon}_{T_{\min}}^{pl} = \dot{\epsilon}_0 g(T) \left( \frac{\sigma}{\sigma_0} \right)^n$$

with  $n = 9.94$ . Two additional creep tests at 150 °C for specimens sampled in R direction were performed in Gariboldi et al. (2016). The results indicate that the difference in creep rates for T and R directions is not significant, Fig. 6.11. This supports the assumption of transversely-isotropic creep made in Naumenko and Gariboldi (2014).

### 6.3.1.3 Constitutive Model

In what follows let us assume that the minimum creep rates in R and T directions are approximately the same and the plane spanned on R and T directions to be the isotropy plane. Constitutive equations of transversely-isotropic steady-state creep were applied in Betten (2008) to modeling deep drawing sheets and in Naumenko and Altenbach (2005) to characterize multi-pass weld metals, for example. Let  $\mathbf{e}_L$  be the unit vector that designates the direction L,  $\mathbf{I}$  the second rank unit tensor and  $\mathbf{P} = \mathbf{I} - \mathbf{e}_L \otimes \mathbf{e}_L$  the projector onto the RT plane. For anisotropic materials different parts of the stress state cause different creep responses. Therefore let us decompose the stress state characterized by the stress tensor  $\boldsymbol{\sigma}$  into the three parts including the tension (compression) along L  $\sigma_{LL}$ , the plane stress state in the RT-plane  $\boldsymbol{\sigma}_p$  and the out of plane shear characterized by the shear stress vector  $\boldsymbol{\tau}_L$ . Figure 6.12 illustrates the corresponding components of the stress tensor. The decomposition has the following form

$$\boldsymbol{\sigma} = \sigma_{LL} \mathbf{e}_L \otimes \mathbf{e}_L + \boldsymbol{\sigma}_p + \boldsymbol{\tau}_L \otimes \mathbf{e}_L + \mathbf{e}_L \otimes \boldsymbol{\tau}_L \quad (6.3.38)$$

By subtracting the hydrostatic stress state the stress deviator  $\mathbf{s}$  can be given as follows

$$\mathbf{s} = \mathbf{s}_L + \mathbf{s}_p + \boldsymbol{\tau}_L \otimes \mathbf{e}_L + \mathbf{e}_L \otimes \boldsymbol{\tau}_L, \quad (6.3.39)$$

where

$$\mathbf{s}_L = \left( \sigma_{LL} - \frac{1}{2} \text{tr} \boldsymbol{\sigma}_p \right) \left( \mathbf{e}_L \otimes \mathbf{e}_L - \frac{1}{3} \mathbf{I} \right), \quad \mathbf{s}_p = \boldsymbol{\sigma}_p - \frac{1}{2} \text{tr} \boldsymbol{\sigma}_p (\mathbf{I} - \mathbf{e}_L \otimes \mathbf{e}_L) \quad (6.3.40)$$

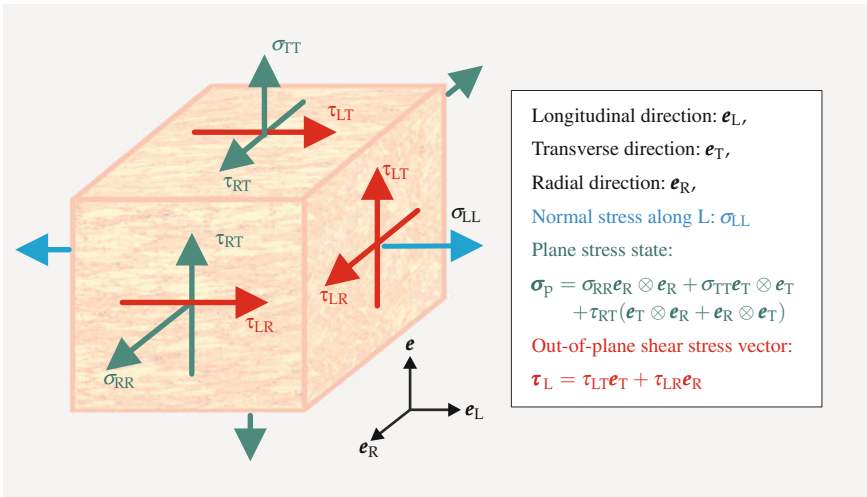


**Fig. 6.12** Stress state in a forged material with elongated grains and preference (forging) direction  $\mathbf{m} = \mathbf{e}_L$ , after Naumenko and Gariboldi (2014)

With the decomposition (6.3.39), the creep potential hypothesis and the assumption that the volumetric creep rate is negligible, the constitutive equation can be formulated as follows, see Sect. 5.4.3.1

$$\dot{\boldsymbol{\varepsilon}}^{\text{pl}} = \frac{3}{2} \dot{\varepsilon}_0 g(T) \left( \frac{\sigma_{\text{eq}}}{\sigma_0} \right)^n \frac{1}{\sigma_{\text{eq}}} \left[ \alpha_1 \mathbf{s}_L + \alpha_2 \mathbf{s}_p + \alpha_3 (\boldsymbol{\tau}_L \otimes \mathbf{e}_L + \mathbf{e}_L \otimes \boldsymbol{\tau}_L) \right], \quad (6.3.41)$$

where  $\boldsymbol{\varepsilon}^{\text{pl}}$  is the tensor of inelastic strains,  $\dot{\varepsilon}_0$ ,  $\sigma_0$ ,  $n$  and  $\alpha_i$ ,  $i = 1, 2, 3$  are material parameters. The equivalent stress  $\sigma_{\text{eq}}$  is defined as follows

$$\sigma_{\text{eq}}^2 = \frac{3}{2} \left( \alpha_1 \text{tr} \mathbf{s}_L^2 + \alpha_2 \text{tr} \mathbf{s}_p^2 + 2\alpha_3 \boldsymbol{\tau}_L \cdot \boldsymbol{\tau}_L \right) \quad (6.3.42)$$

To identify the material parameters families of creep curves for different stress levels for three independent kinds of loading are required. These include the loading in L and T directions, respectively as well as any kind of loading that leads to non-zero out-of-plane shear stress. For  $\alpha_1 = \alpha_2 = \alpha_3 = 1$  the von Mises equivalent stress follows from Eq. (6.3.42). Equation (6.3.41) reduces to the Norton-Bailey-Odqvist equation of isotropic creep in the power law range (5.4.107).

For the tensile stress  $\sigma_{LL}$  the longitudinal creep rate  $\dot{\varepsilon}_{\text{TT}}^{\text{pl}}$  can be computed from Eq. (6.3.41) as follows

$$\dot{\varepsilon}_{\text{LL}}^{\text{pl}} = \dot{\varepsilon}_0 g(T) \left( \frac{\sigma_{LL}}{\sigma_0} \right)^n \alpha_1^{\frac{n+1}{2}} \quad (6.3.43)$$

The creep rate in the transverse direction for the applied stress  $\sigma_{\text{TT}}$  is

$$\dot{\varepsilon}_{\text{TT}}^{\text{pl}} = \dot{\varepsilon}_0 g(T) \left( \frac{\sigma_{\text{TT}}}{\sigma_0} \right)^n \left( \frac{\alpha_1 + 3\alpha_2}{4} \right)^{\frac{n+1}{2}} \quad (6.3.44)$$

The function  $g(T)$  and the parameter  $\dot{\varepsilon}_0$  can be identified from minimum creep rate versus stress data generated from transverse creep curves, Fig. 6.11. In this case the parameter  $\alpha_2$  can be set to one. To identify the parameter  $\alpha_1$  the ratio of creep rates  $\alpha$  for the same stress level can be computed from Eqs. (6.3.43) and (6.3.44) as follows

$$\alpha = \frac{\dot{\varepsilon}_{\text{TT}}^{\text{pl}}}{\dot{\varepsilon}_{\text{LL}}^{\text{pl}}} = \left( \frac{\alpha_1 + 3}{4\alpha_1} \right)^{\frac{n+1}{2}} \quad (6.3.45)$$

For the given values of  $\alpha$  and  $n$  the solution of Eq. (6.3.45) is  $\alpha_1 = 0.81$ .

### 6.3.2 *Multi-pass Weld Metal*

For many structures designed for high-temperature applications, e.g., piping systems and pressure vessels, an important problem is the assessment of creep strength of welded joints. The lifetime of the welded structure is primarily determined by the behavior in the local zones of welds, where time-dependent creep and damage processes dominate. Different types of creep failure that have occurred in recent years are discussed in Shibli (2002), for example. The design of welded structures and their residual life estimations require engineering mechanics models that would be able to characterize creep strains, stress redistributions, and damage evolution in the zones of welds.

A weld is usually considered as a metallurgical notch. The reason for this is the complex microstructure in the weld metal itself and in the neighboring heat-affected zone. Many research activities have been directed to the study of welded joints. First, theoretical and experimental studies have addressed the welding process with the aim of predicting the formation of the microstructure of the welds and analyzing residual stresses (Aurich et al. 1999). Second, the behavior of welded joints under the mechanical and thermal loadings was investigated (Hyde et al. 2003b). Here one must consider that the stress-strain response at room temperature is quite different for the weld metal, the heat-affected zone, and the base metal (parent material), particularly if they are loaded beyond the yield limit. At elevated temperatures quite different inelastic strain versus time curves can be obtained in different zones even in the case of a constant moderate load. Figure 1.52 illustrates zones with different microstructures and the variation in material behavior within the weld.

The results of creep tests of cross-weld specimens (Hyde et al. 1997, 1999), and specimens with a simulated microstructure (Lundin et al. 2001; Matsui et al. 2001; Wohlfahrt and Brinkmann 2001; Wu et al. 2004) show significant variation in creep properties in different material zones within the weld. Furthermore, they illustrate that the intercritical region of the heat-affected zone is the weakest part of the weld with respect to the creep properties. The material with the heat-affected zone microstructure usually exhibits the highest creep rate and the shortest time to failure if compared to other material zones within the weld for the same load and temperature.

For thick and moderately thick cross sections, multi-pass welding is usually preferred, where many stringer beads are deposited in a defined sequence. As a result of heating and cooling cycles during the welding process, the complex bead-type microstructure of the weld metal is formed, where every single bead consists of columnar, coarse-grained, and fine-grained regions (Hyde et al. 2003b). The results of uni-axial creep tests for the weld metal 9CrMoNbV are reported in Hyde et al. (2003a). They show that the creep strain versus time curves significantly differ for specimens removed from the weld metal in the longitudinal (welding) direction and the transverse direction. Furthermore, different types of damage were observed for the longitudinal and the transverse specimens.

One possibility for studying the creep behavior in structures is the use of continuum damage mechanics (Altenbach and Naumenko 2002; Altenbach et al. 2001; Hayhurst 1994). The application of this approach to welded joints is discussed in Hall and Hayhurst (1991), Hayhurst et al. (2002), Hyde et al. (2003b), for example. Here the weld is considered as a heterogeneous structure composed of at least three constituents—the weld metal, the heat-affected zone, and the parent material with different creep properties. Constitutive and evolution equations that are able to reflect experimental data of primary, secondary, and tertiary creep in different zones of the welded joint are presented in Eggeler et al. (1994), Hall and Hayhurst (1991), Hayhurst et al. (2002), Hyde et al. (2003b), Wohlfahrt and Brinkmann (2001), among others. The results of finite element simulations illustrate stress redistributions, creep strains, and damage evolution in different zones of the weld (Eggeler et al. 1994; Hall and Hayhurst 1991; Hayhurst et al. 2002; Hyde et al. 2003b). Furthermore, they are useful to analyze the influence of numerous factors like weld dimensions, types of external loading, and material properties on the creep behavior of welded structures (Hyde et al. 2003b).

### 6.3.2.1 Basic Features of Microstructure

A weld bead produced by a single pass welding has a columnar solidification microstructure. During the multi-pass welding many weld beads are deposited in the groove by a defined sequence. As a subsequent weld bead is laid, the part of the metal produced in previous cycles is subjected to the local reheating and cooling. As a result, the weld beads consist of columnar, coarse-grained and fine-grained microstructural zones (Hyde et al. 2003a, b). A sketch for the typical microstructure of a multi-pass weld metal is presented in Fig. 6.13. This microstructure depends on many factors of the welding process like bead size, travel speed, buildup sequence, interpass temperature, and type of postweld heat treatment (Hyde et al. 2003a). The resulting inelastic material behavior will be apparently determined by the distribution and size of columnar, coarse-grained, and fine-grained zones as well as residual stresses in the weld metal. It is well established that creep behavior is very sensitive to the type of microstructure and, in particular, to grain size. Experimental data illustrating the significant influence of grain size on creep behavior are presented for copper in Kowalewski (1992) and for various types of steel in Lundin et al. (2001), Wohlfahrt and Brinkmann (2001), Wu et al. (2004). The grain size dependence is explained in materials science by two creep mechanisms: grain boundary sliding and grain boundary diffusion. These mechanisms operate under moderate loading and within a temperature range of  $0.5 < T/T_m < 0.7$ , where  $T_m$  is the melting temperature (see Sect. 1.3). The principal damage mechanism is the nucleation and growth of voids on grain boundaries. Many experimental observations show that the finer the grain structure, the higher the secondary creep rate and the higher the damage rate for the same loading and temperature conditions.

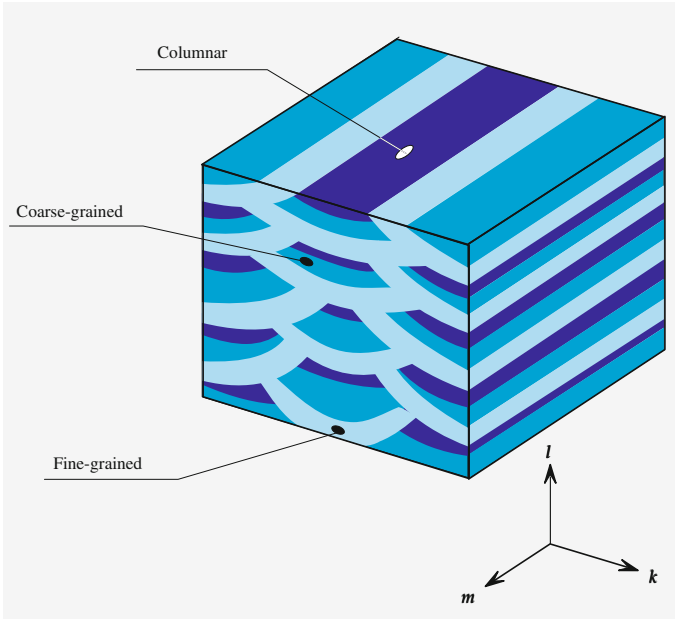


Fig. 6.13 Microstructure of the weld metal, after Naumenko and Altenbach (2005)

### 6.3.2.2 Elementary Micromechanics Model

To discuss the origins of the anisotropic creep in a weld metal let us consider a uni-axial model of a binary structure composed of constituents with different creep properties. In what follows let us term the first constituent “fine-grained” or “creep-weak” and the second one “coarse-grained” or “creep-strong.” Let us describe the creep behavior of the constituents by use of the Kachanov-Rabotnov model (see Sect. 3.6.1)

$$\dot{\epsilon}^{pl} = \frac{a\sigma^n}{(1 - \omega)^n}, \quad \dot{\omega} = \frac{b\sigma^k}{(1 - \omega)^l} \tag{6.3.46}$$

In what follows we use the subscripts f and c for the fine-grained and coarse-grained constituents, respectively. For the sake of simplicity we assume that the constituents have the same value of Young’s modulus  $E$  and the same values of parameters  $n, k$  and  $l$  in (6.3.46). Let us introduce the dimensionless quantities

$$s = \frac{\sigma}{\sigma_0}, \quad \epsilon = \frac{\epsilon}{\epsilon_0}, \quad \epsilon^{pl} = \frac{\epsilon^{pl}}{\epsilon_0}, \quad \tau = \frac{t}{t_{*f}}, \tag{6.3.47}$$

where  $t_{*f}$  is the time to fracture of the fine-grained constituent,  $\sigma_0$  is the reference stress and  $\epsilon_0$  is the elastic strain at  $\sigma_0$ , i.e.  $\epsilon_0 = \sigma_0/E$ . Equations (6.3.46) can be formulated for two constituents as follows

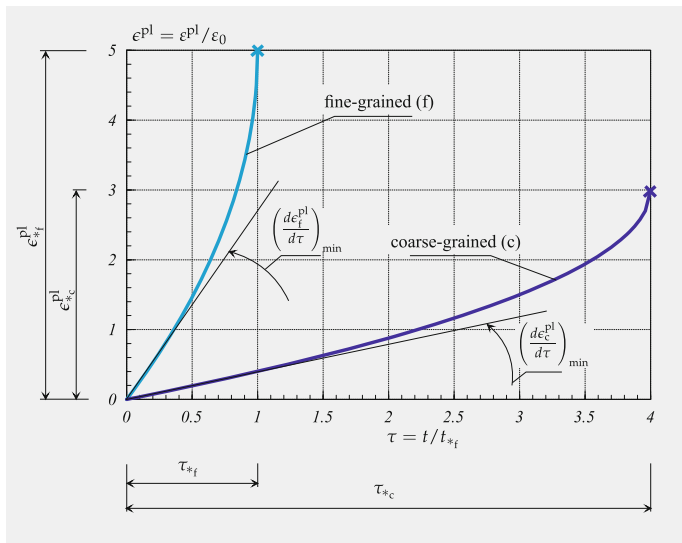


**Fig. 6.14** Creep curves for constituents

$$\begin{cases} \frac{d\epsilon_f^{\text{pl}}}{d\tau} = \tilde{a} \frac{s^n}{(1-\omega_f)^n} \\ \frac{d\omega_f}{d\tau} = \tilde{b} \frac{s^k}{(1-\omega_f)^l} \end{cases}, \quad \begin{cases} \frac{d\epsilon_c^{\text{pl}}}{d\tau} = \alpha \tilde{a} \frac{s^n}{(1-\omega_c)^n} \\ \frac{d\omega_c}{d\tau} = \beta \tilde{b} \frac{s^k}{(1-\omega_c)^l} \end{cases}, \quad (6.3.48)$$

where

$$\tilde{a} = \epsilon_{*f} \left(1 - \frac{n}{l+1}\right), \quad \tilde{b} = \frac{1}{l+1}, \quad \alpha = \frac{\dot{\epsilon}_{\text{min}_c}^{\text{pl}}}{\dot{\epsilon}_{\text{min}_f}^{\text{pl}}}, \quad \beta = \frac{t_{*f}}{t_{*c}}$$

Figure 6.14 illustrates creep curves obtained after integration of Eqs. (6.3.48) for the cases  $n = 3$ ,  $k = n + 1$ ,  $l = n + 2$ ,  $\epsilon_{*f} = 5$ ,  $\alpha = 0.15$ ,  $\beta = 0.25$ ,  $s = 1$ .

Let us consider a connection of constituents in parallel, as it usually assumed for composite materials (Altenbach et al. 2004; Chawla 1987). The strains and the strain rates can be assumed to be the same (iso-strain concept)

$$\epsilon = \epsilon_f = \epsilon_c, \quad \dot{\epsilon} = \dot{\epsilon}_f = \dot{\epsilon}_c \quad (6.3.49)$$

We assume that a constant load  $\mathcal{F} = \sigma_0 A$ , Fig. 6.15, is applied to the composite, where  $A$  is the cross section area. Specifying by  $N_f$  and  $N_c$  the internal forces in the constituents such that  $N_f + N_c = \mathcal{F}$  we can write

$$\sigma_f A_f + \sigma_c A_c = \sigma_0 A, \quad \eta_f \sigma_f + (1 - \eta_f) \sigma_c = \sigma_0, \quad \eta_f s_f + (1 - \eta_f) s_c = 1 \quad (6.3.50)$$

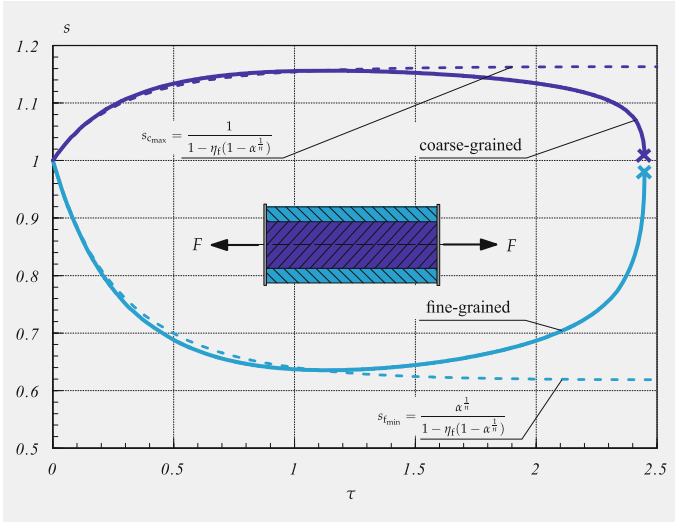


**Fig. 6.15** Normalized stresses versus normalized time for connection of constituents in parallel

where  $\eta_f = A_f/A$  is the volume fraction of the fine-grained constituent. For the stresses we apply the following constitutive equations

$$\sigma_f = E(\varepsilon - \varepsilon_f^{\text{pl}}), \quad \sigma_c = E(\varepsilon - \varepsilon_c^{\text{pl}}) \quad (6.3.51)$$

Based on Eqs. (6.3.48)–(6.3.51) one can formulate a system of ordinary differential equations describing the stress redistribution between constituents. With respect to the stress in the fine-grained constituent the following equation can be obtained

$$\frac{ds_f}{d\tau} = \bar{a}(1 - \eta_f) \left[ \frac{\alpha}{(1 - \eta_f)^n} \frac{(1 - \eta_f s_f)^n}{(1 - \omega_c)^n} - \frac{s_f^n}{(1 - \omega_f)^n} \right] \quad (6.3.52)$$

Equation (6.3.52) is numerically solved together with the evolution equations for the damage parameters (6.3.48) and initial conditions  $s_f = 1$ ,  $\omega_f = \omega_c = 0$  providing time variation of the stress  $s_f$ . The stress  $s_c$  can be then computed from Eqs. (6.3.50). The results are shown in Fig. 6.15 for the case  $\eta_f = 0.3$ . In addition, Fig. 6.16 presents creep strains and the damage parameters in the constituents as well as the creep strain of the mixture  $\varepsilon^{\text{pl}} = \varepsilon - 1$ . At the beginning of the creep process the creep rate is higher in the fine-grained constituent, Fig. 6.16a. Therefore, the stress in the fine-grained constituent relaxes down while the stress in the coarse-grained constituent increases, Fig. 6.15. If we neglect the influence of damage on the creep process, i.e. set  $\omega_f = \omega_c = 0$  in (6.3.52), we obtain the steady-state creep solution. The corresponding results are plotted in Fig. 6.15 by dotted lines. We observe that the maximum value of  $s_c$  and the minimum value of  $s_f$  in the case of creep-damage almost coincide with the corresponding steady-state values. The steady-state solution for  $s_f$  follows from Eqs. (6.3.52) by setting  $\omega_f = \omega_c = 0$  and  $\frac{ds_f}{d\tau} = 0$ . The corresponding

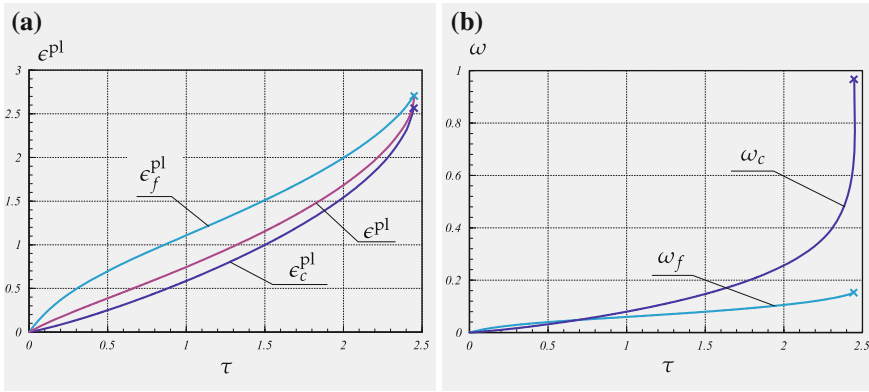


**Fig. 6.16** Connection of constituents in parallel. **a** Normalized creep strains versus normalized time, **b** damage parameters versus normalized time

value for  $s_c$  is obtained from (6.3.50). The results are

$$s_{f_{\min}} = \frac{\alpha^{\frac{1}{n}}}{1 - \eta_f(1 - \alpha^{\frac{1}{n}})}, \quad s_{c_{\max}} = \frac{1}{1 - \eta_f(1 - \alpha^{\frac{1}{n}})}$$

We observe that these stress values are determined by the volume fraction of the “fine-grained” constituent  $\eta_f$  and the ratio of minimum creep rates  $\alpha$ . The stress value  $s_c$  is higher than  $s_f$  after the initial stress redistribution. Therefore, the coarse-grained constituent exhibits the higher creep rate and the higher damage rate in the final stage of the creep process, Fig. 6.16. The simulation predicts the failure initiation in the coarse-grained constituent.

In the case of a connection of constituents in series (iso-stress approach) we assume

$$\sigma_0 = \sigma_f = \sigma_c, \quad \varepsilon^{\text{pl}} = \eta_f \varepsilon_f^{\text{pl}} + (1 - \eta_f) \varepsilon_c^{\text{pl}}$$

The results can be obtained by integration (6.3.48) for  $s_f = s_c = 1$ . The corresponding plots of normalized creep strains are presented in Fig. 6.14. The maximum creep and damage rates are now in the fine-grained constituent. The lifetime of the binary structure is determined by the lifetime of the fine-grained constituent for the given constant stress.

Figure 6.17 shows the creep curves obtained for the two considered cases of the binary structure under the same constant load. The results of the presented model provide an analogy to the creep behavior of a weld metal loaded in the longitudinal (welding) and the transverse directions. The experimental creep curves for the specimen removed from the weld metal in two directions are presented in Hyde et al. (2003a). They show, that the transverse specimens exhibit higher minimum creep rate. Furthermore, the creep curves for transverse specimens have a much shorter tertiary stage and lower values of fracture strain if compared to curves for specimens removed in the welding direction. The times to fracture for the transverse speci-

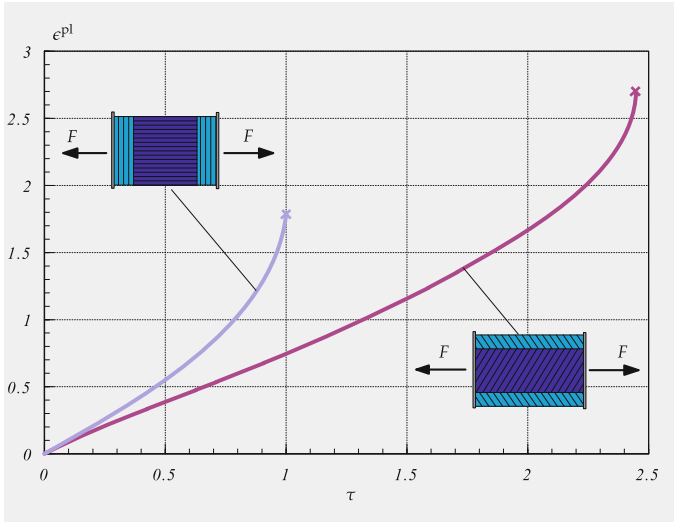


**Fig. 6.17** Creep curves for the binary structure in the cases of parallel and series connections of constituents

mens are much shorter than those for the longitudinal specimens. From the results in Fig. 6.17 we observe that these effects are predicted by the mechanical model of the binary structure. Furthermore, our results for the damage evolution qualitatively agree with the results of microstructural damage observations presented in Hyde et al. (2003a). For the longitudinal specimens extensive voids and cracks were observed in columnar and coarse-grained regions along the entire specimen length. For the transverse specimens voids and cracks are localized near the fracture surface. The fracture surface has fine-grained structure and the failure propagated through the fine-grained regions of the specimen.

Based on the presented results we may conclude that among many different creep and damage mechanisms which may operate and interact during the creep process an essential role plays the stress redistribution between the creep-weak and creep-strong constituents. For longitudinal specimens this mechanism leads to a prolonged tertiary creep stage. The material behaves like a “more ductile” material, although the damage and failure occur in the “more brittle” creep-strong constituent.

In Hyde and Sun (2005), Lvov et al. (2014) micromechanical models of multi-pass weld are presented by taking into account realistic distributions of weld beads and microstructural zones. Finite element simulations of the weld metal sample are performed for different stress states including tension in welding and transverse directions as well a longitudinal and transverse shear.

### 6.3.2.3 Constitutive Model

For the analysis of welded structures a model which is able to reflect anisotropic creep in a weld metal under multi-axial stress states has to be developed. Three-dimensional models for mixtures are discussed within the framework of continuum mechanics, e.g. Altenbach et al. (2003). A generalization of the composite model developed in the previous section to the multi-axial stress states would however require the knowledge of creep properties of constituents under multi-axial stress states. Furthermore, creep mechanisms of interaction between constituents, like frictional sliding should be taken into account.

In what follows we assume the weld metal to be a quasi-homogeneous anisotropic material. For a description of creep we prefer the engineering creep mechanics approach, where the creep potential hypothesis, the representation of tensor functions and internal state variables are applied (see Sect. 5.4.3). The resulting constitutive equations can be utilized in standard finite element codes for structural analysis purposes.

Examples for anisotropic creep behavior and related constitutive equations are presented for a single-crystal alloy in Bertram and Olschewski (2001), a fiber-reinforced material in Robinson et al. (2003) and a forged aluminium alloy in Sect. 6.3.1. One problem of anisotropic creep modeling is that the assumed material symmetries (microstructure symmetries) are difficult to verify in creep tests due to the relatively large scatter of experimental data. Furthermore, the material may lose some or even all symmetries during the creep as a consequence of hardening and damage processes.

In our case the material symmetries can be established according to the arrangement of the weld beads in the weld metal. For the structure presented in Fig. 6.13 one can assume the reflection  $\mathbf{Q}_1 = \mathbf{I} - 2\mathbf{m} \otimes \mathbf{m}$ , the rotation  $\mathbf{Q}_2 = 2\mathbf{l} \otimes \mathbf{l} - \mathbf{I}$  and the reflection  $\mathbf{Q}_3 = \mathbf{Q}_1 \cdot \mathbf{Q}_2 = \mathbf{I} - 2\mathbf{k} \otimes \mathbf{k}$  to be the elements of the material symmetry group, where  $\mathbf{I}$  is the second rank unit tensor and  $\mathbf{k}$ ,  $\mathbf{l}$  and  $\mathbf{m}$  are orthogonal unit vectors.

However, this material symmetry group is poor for the modeling of creep. Indeed, based on the model discussed in the previous section we can assume that the same creep mechanisms will operate by loading the weld metal in  $\mathbf{k}$ - or  $\mathbf{l}$ -directions. Although the experimental data presented in Hyde et al. (2003a) are available only for specimen removed in  $\mathbf{m}$ - and  $\mathbf{k}$ -directions, one may assume that the difference between the experimental creep curves by loading in  $\mathbf{k}$ - and  $\mathbf{l}$ -directions will be not essential with respect to the usual scatter of experimental data. Here we assume transversely isotropic creep, where the plane spanned on the vectors  $\mathbf{k}$  and  $\mathbf{l}$  is the quasi-isotropy plane.

The models of steady-state creep under the assumption of transverse isotropy are derived in Sects. 5.4.3.1 and 5.4.3.2. Here we apply the constitutive Eq. (5.4.139). In the equivalent stress expression (5.4.137) the  $\alpha_i$ 's play the role of dimensionless factors. Three independent uniform stress states should be realized in order to determine  $\alpha_i$ . The relevant stress states are

- Uni-axial tension in the direction  $\mathbf{m}$  (longitudinal tension test). In this case the stress tensor is  $\boldsymbol{\sigma} = \sigma_0 \mathbf{m} \otimes \mathbf{m}$ , where  $\sigma_0 > 0$  is the magnitude of the applied stress. From Eqs. (5.4.137) and (5.4.139) follows

$$\begin{aligned} J_m &= \sigma_0, \quad I_{3m} = I_{4m} = 0, \quad \sigma_{\text{eq}} = \sigma_0 \sqrt{\alpha_1}, \\ \dot{\boldsymbol{\varepsilon}}^{\text{pl}} &= \sqrt{\alpha_1} \dot{\varepsilon}_{\text{eq}} \left[ \mathbf{m} \otimes \mathbf{m} - \frac{1}{2} (\mathbf{I} - \mathbf{m} \otimes \mathbf{m}) \right] \end{aligned} \quad (6.3.53)$$

- Uni-axial tension in the direction  $\mathbf{k}$  (transverse tension test), i.e.  $\boldsymbol{\sigma} = \sigma_0 \mathbf{k} \otimes \mathbf{k}$ ,  $\sigma_0 > 0$ . From Eqs. (5.4.137) and (5.4.139) we obtain

$$\begin{aligned} \mathbf{s}_p &= \frac{1}{2} \sigma_0 (\mathbf{k} \otimes \mathbf{k} - \mathbf{l} \otimes \mathbf{l}), \quad J_m = -\frac{1}{2} \sigma_0, \\ I_{3m} &= \frac{1}{4} \sigma_0^2, \quad I_{4m} = 0, \quad \sigma_{\text{eq}} = \frac{1}{2} \sigma_0 \sqrt{\alpha_1 + 3\alpha_2}, \\ \dot{\boldsymbol{\varepsilon}}^{\text{pl}} &= \frac{\dot{\varepsilon}_{\text{eq}}}{2\sqrt{\alpha_1 + 3\alpha_2}} [(\alpha_1 + 3\alpha_2) \mathbf{k} \otimes \mathbf{k} + (\alpha_1 - 3\alpha_2) \mathbf{l} \otimes \mathbf{l} - 2\alpha_1 \mathbf{m} \otimes \mathbf{m}] \end{aligned} \quad (6.3.54)$$

- Uniform shear in the plane spanned on  $\mathbf{m}$  and  $\mathbf{k}$ , i.e.  $\boldsymbol{\sigma} = \tau_0 (\mathbf{m} \otimes \mathbf{k} + \mathbf{k} \otimes \mathbf{m})$ ,  $\tau_0 > 0$ . From Eqs. (5.4.137) and (5.4.139)

$$J_m = I_{3m} = 0, \quad I_{4m} = \tau_0^2, \quad \dot{\boldsymbol{\varepsilon}}^{\text{pl}} = \frac{\sqrt{3\alpha_3}}{2} \dot{\varepsilon}_{\text{eq}} (\mathbf{m} \otimes \mathbf{k} + \mathbf{k} \otimes \mathbf{m}) \quad (6.3.55)$$

The next step is the form of the creep potential  $W(\sigma_{\text{eq}})$  or the form of the creep rate versus stress dependence in the steady-state range. The criteria for the choice of a suitable function are the type of the deformation mechanisms operating for the given stress and temperature range as well as the best fitting of the experimentally obtained strain versus time curves. Experimental data for the weld metal 9CrMoNbV are presented in Hyde et al. (2003a) for the stress range 87–100 MPa and the constant temperature 650 °C. The authors used a power law in order to fit the experimental data for secondary creep of longitudinal and transverse specimens. In this case the Norton-Bailey-Odqvist creep potential can be applied (Odqvist and Hult 1962)

$$W(\sigma_{\text{eq}}) = \frac{a}{n+1} \sigma_{\text{eq}}^{n+1}, \quad \dot{\varepsilon}_{\text{eq}} = a \sigma_{\text{eq}}^n, \quad (6.3.56)$$

where  $a$  and  $n$  are material parameters. For the longitudinal direction from Eqs. (6.3.53) and (6.3.56) it follows

$$\dot{\varepsilon}_L^{\text{pl}} \equiv \mathbf{m} \cdot \dot{\boldsymbol{\varepsilon}}^{\text{pl}} \mathbf{m} = a_L \sigma_0^n, \quad a_L \equiv a \alpha_1^{\frac{n+1}{2}} \quad (6.3.57)$$

Taking the longitudinal direction to be the “reference” direction we set in Eqs. (6.3.57)  $\alpha_1 = 1$ . From Eqs. (6.3.54) and (6.3.56) we obtain for the transverse direction

$$\dot{\epsilon}_T^{pl} \equiv \mathbf{k} \cdot \dot{\epsilon}^{pl} \cdot \mathbf{k} = a_T \sigma_0^n, \quad a_T \equiv a \left( \frac{1 + 3\alpha_2}{4} \right)^{\frac{n+1}{2}} \tag{6.3.58}$$

In Hyde et al. (2003a) the values for the material parameters are presented. However, the exponent  $n$  is found to be different for the longitudinal and the transverse directions. Different values for  $n$  contradict to the creep potential hypothesis employed in the previous section. Here we compute the values for  $a_L$ ,  $a_T$  and  $n$  based on the following functional

$$F(\tilde{a}_L, \tilde{a}_T, n) = \sum_{i=1}^k (\tilde{a}_L + n\tilde{\sigma}_i - \tilde{\epsilon}_{L_i})^2 + \sum_{i=1}^k (\tilde{a}_T + n\tilde{\sigma}_i - \tilde{\epsilon}_{T_i})^2, \tag{6.3.59}$$

$$\tilde{a}_L \equiv \log a_L, \quad \tilde{a}_T \equiv \log a_T, \quad \tilde{\sigma} \equiv \log \sigma_0,$$

$$\tilde{\epsilon}_L \equiv \log \dot{\epsilon}_L, \quad \tilde{\epsilon}_T \equiv \log \dot{\epsilon}_T,$$

where  $k$  is the number of experimental data points. Setting the first variation of  $F$  to zero leads to the system of three algebraic equations with respect to  $\tilde{a}_L$ ,  $\tilde{a}_T$  and  $n$ . As the result we obtain the following set of material constants

$$a_L = 1.377 \cdot 10^{-21} \text{ MPa}^{-n} / \text{h}, \quad a_T = 2.023 \cdot 10^{-21} \text{ MPa}^{-n} / \text{h}, \tag{6.3.60}$$

$$n = 8.12$$

Figure 6.18 shows the experimental data presented in Hyde et al. (2003a) and the numerical predictions by use of Eqs. (6.3.57), (6.3.58) and (6.3.60).

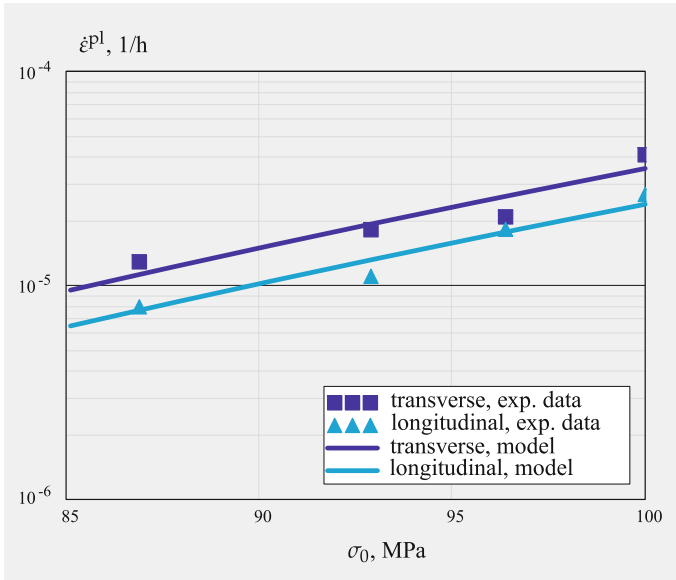


Fig. 6.18 Minimum creep rates versus stress, experimental data after Hyde et al. (2003a)

Finally let us summarize the constitutive equation for secondary creep and the set of identified material constants as follows

$$\begin{aligned}\dot{\boldsymbol{\epsilon}}^{\text{pl}} &= \frac{3}{2} a \sigma_{\text{eq}}^{n-1} \left[ J_m \left( \mathbf{m} \otimes \mathbf{m} - \frac{1}{3} \mathbf{I} \right) + \alpha_2 \mathbf{s}_p + \alpha_3 (\boldsymbol{\tau}_m \otimes \mathbf{m} + \mathbf{m} \otimes \boldsymbol{\tau}_m) \right], \\ \sigma_{\text{eq}}^2 &= \left( \mathbf{m} \cdot \boldsymbol{\sigma} \cdot \mathbf{m} - \frac{1}{2} \text{tr} \boldsymbol{\sigma}_p \right)^2 + \frac{3}{2} \alpha_2 \text{tr} \mathbf{s}_p^2 + 3 \alpha_3 \tau_m^2, \\ a &= 1.377 \cdot 10^{-21} \text{ MPa}^{-n} / \text{h}, \quad n = 8.12, \quad \alpha_2 = 1.117\end{aligned}\tag{6.3.61}$$

The weighting factor  $\alpha_3$ , which stands for the influence of the transverse shear stress, remains undetermined in Eqs. (6.3.61) since experimental data of creep under transverse shear stress state are not available. In Lvov et al. (2014) results of micromechanics simulations of a weld metal samples subjected to different stress states are presented. The obtained creep rates indicate that one may set  $\alpha_2 \approx \alpha_3$ .

Model (6.3.61) is limited only to secondary creep behavior and can be used to reproduce only the secondary part of the creep curves presented in Hyde et al. (2003a). For the description of the whole creep process including the primary and tertiary creep stages, model (6.3.61) can be modified by use of hardening, softening and damage variables.

## References

- Abe F (2001) Creep rates and strengthening mechanisms in tungsten-strengthened 9Cr steels. *Mater Sci Eng A319–A321*:770–773
- Abe F (2004) Bainitic and martensitic creep-resistant steels. *Curr Opin Solid State Mater Sci* 8(3):305–311
- Altenbach H, Naumenko K (1997) Creep bending of thin-walled shells and plates by consideration of finite deflections. *Comput Mech* 19:490–495
- Altenbach H, Naumenko K (2002) Shear correction factors in creep-damage analysis of beams, plates and shells. *JSME International Journal Series A, Solid Mechanics and Material Engineering* 45:77–83
- Altenbach H, Altenbach J, Naumenko K (1997a) On the prediction of creep damage by bending of thin-walled structures. *Mech Time-Depend Mater* 1:181–193
- Altenbach H, Morachkovsky O, Naumenko K, Sychov A (1997b) Geometrically nonlinear bending of thin-walled shells and plates under creep-damage conditions. *Arch Appl Mech* 67:339–352
- Altenbach H, Kolarow G, Morachkovsky O, Naumenko K (2000) On the accuracy of creep-damage predictions in thinwalled structures using the finite element method. *Comput Mech* 25:87–98
- Altenbach H, Kushnevsy V, Naumenko K (2001) On the use of solid- and shell-type finite elements in creep-damage predictions of thinwalled structures. *Arch Appl Mech* 71:164–181
- Altenbach H, Naumenko K, Zhilin P (2003) A micro-polar theory for binary media with application to phase-transitional flow of fiber suspensions. *Continuum Mech Thermodyn* 15:539–570
- Altenbach H, Altenbach J, Kissing W (2004) *Mechanics of composite structural elements*. Springer, Berlin
- Altenbach J, Altenbach H, Naumenko K (1997c) Lebensdauerabschätzung dünnwandiger Flächentragwerke auf der Grundlage phänomenologischer Materialmodelle für Kriechen und Schädigung. *Technische Mechanik* 17(4):353–364

- Angella A, Bassani E, Gariboldi E, Ripamonti D (2008) Microstructural stability and related mechanical properties of a Al-Cu-Mg-Si alloy. In: Hirsch J, Skrotzky B, Gottstein G (eds) *Aluminium alloys*, vol 1, Wiley-VCH, pp 1092–1067
- Aurich D, Kloos KH, Lange G, Macherauch E (1999) *Eigenspannungen und Verzug durch Wärmeeinwirkung*. DFG Forschungsbericht, Wiley-VCH, Weinheim
- Bertram A, Olschewski J (2001) A phenomenological anisotropic creep model for cubic single crystals. In: Lemaître J (ed) *Handbook of materials behaviour models*. Academic Press, San Diego, pp 303–307
- Betten J (2008) *Creep Mechanics*, 3rd edn. Springer, Berlin
- Bodnar A, Chrzanowski M (1991) A non-unilateral damage in creeping plates. In: Zyczkowski M (ed) *Creep in Structures*. Springer, Berlin, Heidelberg, pp 287–293
- de Borst R (2004) Damage, material instabilities, and failure. In: Stein E, de Borst R, Hughes TJR (eds) *Encyclopedia of computational mechanics*. John Wiley & Sons, Chichester, pp 335–373
- Boyle JT, Spence J (1983) *Stress analysis for creep*. Butterworth, London
- Chawla KK (1987) *Composite materials*. Springer, New York
- Choudhary BK, Paniraj C, Rao K, Mannan SL (2001) Creep deformation behavior and kinetic aspects of 9Cr-1Mo ferritic steel. *Iron and steel institut of Japan (ISIJ)*. International 41:73–80
- Dyson BF (1996) Mechanical testing of high-temperature materials: modelling data-scatter. In: Cahn RW, Evans AG, McLean M (eds) *High-temperature structural materials*, Chapman & Hall, London, pp 160–192
- Dyson BF, McLean M (2001) Micromechanism-quantification for creep constitutive equations. In: Murakami S, Ohno N (eds) *IUTAM symposium on creep in structures*. Kluwer, Dordrecht, pp 3–16
- Eggeler G, Ramteke A, Coleman M, Chew B, Peter G, Burlibies A, Hald J, Jefferey C, Rantala J, de Witte M, Mohrmann R (1994) Analysis of creep in a welded P91 pressure vessel. *Int J Press Vessels Pip* 60:237–257
- Frost HJ, Ashby MF (1982) *Deformation-mechanism maps*. Pergamon, Oxford
- Gandy D (2006) X20CrMoV12-1 steel handbook. Technical report. Electric Power Research Institute, 1012740, Palo Ato
- Gariboldi E, Casaro F (2007) Intermediate temperature creep behaviour of a forged Al-Cu-Mg-Si-Mn alloy. *Mater Sci Eng: A* 462(1):384–388
- Gariboldi E, Conte A (2013) Effect of orientation and overaging on the creep and creep crack growth properties of 2xxx aluminium alloy forgings. In: *Advanced materials modelling for structures*. Springer, pp 165–175
- Gariboldi E, Naumenko K, Ozhoga-Maslovskaia O, Zappa E (2016) Analysis of anisotropic damage in forged Al-Cu-Mg-Si alloy based on creep tests, micrographs of fractured specimen and digital image correlations. *Mater Sci Eng: A* 652:175–185
- Hall FR, Hayhurst DR (1991) Continuum damage mechanics modelling of high temperature deformation and failure in a pipe weldment. *Proc R Soc Lond A: Math Phys Eng Sci* 433:383–403
- Hayhurst DR (1994) The use of continuum damage mechanics in creep analysis for design. *J Strain Anal Eng Des* 25(3):233–241
- Hayhurst DR (1999) Materials data bases and mechanisms-based constitutive equations for use in design. In: Altenbach H, Skrzypek J (eds) *Creep and damage in materials and structures*. Springer, Wien, New York, pp 285–348, CISM Lecture Notes No. 399
- Hayhurst DR (2001) Computational continuum damage mechanics: its use in the prediction of creep fracture in structures—past, present and future. In: Murakami S, Ohno N (eds) *IUTAM symposium on creep in structures*. Kluwer, Dordrecht, pp 175–188
- Hayhurst DR, Wong MT, Vakili-Tahami F (2002) The use of CDM analysis techniques in high temperature creep failure of welded structures. *JSME Int J Ser A, Solid Mech Mater Eng* 45:90–97
- Hoff NJ (1953) The necking and the rupture of rods subjected to constant tensile loads. *Trans of ASME J Appl Mech* 20(1):105–108
- Hyde T, Sun W, Hyde C (2013) *Applied creep mechanics*. McGraw-Hill Education

- Hyde TH, Sun W (2005) A study of anisotropic creep behaviour of a 9CrMoNbV weld metal using damage analyses with a unit cell model. *Proc Inst Mech Eng, Part L: J Mater Des Appl* 219(4):193–206
- Hyde TH, Sun W, Becker AA, Williams JA (1997) Creep continuum damage constitutive equations for the base, weld and heat-affected zone materials of a service-aged 1/2Cr1/2Mo1/4V:2 1/4Cr1Mo multipass weld at 640°C. *J Strain Anal Eng Des* 32(4):273–285
- Hyde TH, Sun W, Williams JA (1999) Creep behaviour of parent, weld and HAZ materials of new, service aged and repaired 1/2Cr1/2Mo1/4V: 21/4Cr1Mo pipe welds at 640°C. *Mater High Temp* 16(3):117–129
- Hyde TH, Sun W, Becker AA (2000) Failure prediction for multi-material creep test specimens using steady-state creep rupture stress. *Int J Mech Sci* 42:401–423
- Hyde TH, Sun W, Agyakwa PA, Shipeay PH, Williams JA (2003a) Anisotropic creep and fracture behaviour of a 9CrMoNbV weld metal at 650°C. In: Skrzypek JJ, Ganczarski AW (eds) *Anisotropic behaviour of damaged materials*. Springer, Berlin, pp 295–316
- Hyde TH, Sun W, Williams JA (2003b) Creep analysis of pressurized circumferential pipe weldments—a review. *J Strain Anal Eng Des* 38(1):1–29
- Kimura K (2006) 9Cr-1Mo-V-Nb Steel. In: Martienssen W (ed) *Creep properties of heat resistant steels and superalloys*. Springer, Berlin, pp 126–133
- Kimura K, Kushima H, Abe F, Yagi K (1997) Inherent creep strength and long term creep strength properties of ferritic steels. *Mater Sci Eng: A* 234:1079–1082
- Kimura K, Kushima H, Sawada K (2009) Long-term creep deformation properties of 9Cr-1Mo steel. *Mater Sci Eng A* 510–A511:58–63
- Kloc L, Sklenička V (2004) Confirmation of low stress creep regime in 9% chromium steel by stress change creep experiments. *Mater Sci Eng A* 387–A389:633–638
- Kloc L, Sklenička V, Ventruba J (2001) Comparison of low creep properties of ferritic and austenitic creep resistant steels. *Mater Sci Eng A* 319–A321:774–778
- Konkin VN, Morachkovskij OK (1987) Polzuchest' i dlitel'naya prochnost' legkikh splavov, proyavlyayushchikh anizotropnye svoystva (Creep and long-term strength of light alloys with anisotropic properties, in Russ.). *Probl Prochn* 5:38–42
- Kostenko E, Naumenko K (2008) Numerische zeitstandanalyse einer kraftwerkskomponente mit einem kriechschädigungs-werkstoffmodell. 31. FVW/FVHT vortragsveranstaltung, langzeitverhalten wärmefester stähle und hochtemperaturwerkstoffe, stahlinstitut VDEh, düsseldorf, pp 37–46
- Kostenko Y, Lvov G, Gorash E, Altenbach H, Naumenko K (2006) Power plant component design using creep-damage analysis. In: *Proceedings of IMECE2006*, IMECE2006-13710. ASME, Chicago, pp 1–10
- Kostenko Y, Schwass G, Naumenko K (2009a) Creep analysis of power plant components from 1%CrMoV and 10%CrMoV steels. In: Shibli IA, Holdsworth SR (eds) *Creep & fracture in high temperature components*. DEStech Publications, Lancaster, Pennsylvania, pp 797–805
- Kostenko Y, Schwass G, Naumenko K (2009b) Creep analysis of power plant components from 1%CrMoV and 10%CrMoV steels. *OMMI—Oper Maintenance Mater Issue* 6(2):1–10
- Kostenko Y, Almstedt H, Naumenko K, Linn S, Scholz A (2013) Robust methods for creep fatigue analysis of power plant components under cyclic transient thermal loading. In: *ASME turbo expo 2013: turbine technical conference and exposition*. American Society of Mechanical Engineers, pp V05BT25A040–V05BT25A040
- Kowalewski Z (1992) The role of grain size on creep of copper under uniaxial tension. *Arch Metall* 37:65–76
- Kowalewski ZL (1996) Creep rupture of copper under complex stress state at elevated temperature. Design and life assessment at high temperature. *Mechanical Engineering Publ*, London, pp 113–122
- Kowalewski ZL, Hayhurst DR, Dyson BF (1994) Mechanisms-based creep constitutive equations for an aluminium alloy. *J Strain Anal Eng Des* 29(4):309–316

- Längler F, Naumenko K, Altenbach H, Ievdokymov M (2014) A constitutive model for inelastic behavior of casting materials under thermo-mechanical loading. *J Strain Anal Eng Des* 49:421–428
- Lemaitre J (1996) *A course on damage mechanics*. Springer, Berlin
- Lemaitre J, Chaboche JL (1990) *Mechanics of solid materials*. Cambridge University Press, Cambridge
- Lin J, Liu Y, Dean TA (2005) A review on damage mechanisms, models and calibration methods under various deformation conditions. *Int J Damage Mech* 14:299–319
- Liu Y, Murakami S, Kageyama Y (1994) Mesh-dependence and stress singularity in finite element analysis of creep crack growth by continuum damage mechanics approach. *Eur J Mech A Solids* 35(3):147–158
- Lundin CD, Liu P, Prager M (2001) Creep behavior of weld heat affected zone regions for modified 9Cr-1Mo Steel. In: *Proceedings of CREEP7*. Japan Society of Mechanical Engineers, Tsukuba, pp 379–382
- Lvov I, Naumenko K, Altenbach H (2014) Homogenisation approach in analysis of creep behaviour in multipass weld. *Mater Sci Technol* 30(1):50–53
- Mahnken R, Stein E (1996) Parameter identification for viscoplastic models based on analytical derivatives of a least-squares functional and stability investigations. *Int J Plast* 12(4):451–479
- Mahnken R, Stein E (1997) Parameter identification for finite deformation elasto-plasticity in principal directions. *Comput Methods Appl Mech Eng* 147(1):17–39
- Maile K, Scheck R (2008) Kriechschädigungsentwicklung in 9–11%Cr Stählen. 31. FVW/FVHT Vortragsveranstaltung, Langzeitverhalten warmfester Stähle und Hochtemperaturwerkstoffe, Stahlinstitut VDEh, Düsseldorf, pp 15–26
- Malinin NN (1981) Raschet na polzuchest' konstrukcionnykh elementov (Creep calculations of structural elements, in Russ.). Mashinostroenie, Moskva
- Matsui M, Tabuchi M, Watanabe T, Kubo K, Kinugawa J, Abe F (2001) Degradation of creep strength in welded joint of 9%cr steel. *Iron Steel Inst Japan (ISIJ) Int* 41:S126–S130
- Mayer KH, Masuyama F (2008) The development of creep-resistant steels. In: Abe F, Kern TU, Viswanathan R (eds) *Creep-resistant steels*. Woodhead Publishing, Cambridge, pp 15–77
- Murakami S, Sanomura Y (1985) Creep and creep damage of copper under multiaxial states of stress. In: Sawczuk A, Bianchi B (eds) *Plasticity today—modelling, methods and applications*. Elsevier, London, New York, pp 535–551
- Naumenko K, Altenbach H (2005) A phenomenological model for anisotropic creep in a multi-pass weld metal. *Arch Appl Mech* 74:808–819
- Naumenko K, Altenbach H (2007) *Modelling of creep for structural analysis*. Springer, Berlin et al
- Naumenko K, Gariboldi E (2014) A phase mixture model for anisotropic creep of forged Al-Cu-Mg-Si alloy. *Mater Sci Eng: A* 618:368–376
- Naumenko K, Kostenko Y (2009) Structural analysis of a power plant component using a stress-range-dependent creep-damage constitutive model. *Mater Sci Eng A* 510–A511:169–174
- Naumenko K, Altenbach H, Gorash Y (2009) Creep analysis with a stress range dependent constitutive model. *Arch Appl Mech* 79:619–630
- Naumenko K, Altenbach H, Kutschke A (2011a) A combined model for hardening, softening and damage processes in advanced heat resistant steels at elevated temperature. *Int J Damage Mech* 20:578–597
- Naumenko K, Kutschke A, Kostenko Y, Rudolf T (2011b) Multi-axial thermo-mechanical analysis of power plant components from 9–12%Cr steels at high temperature. *Eng Fract Mech* 78:1657–1668
- Odqvist FKG (1974) *Mathematical theory of creep and creep rupture*. Oxford University Press, Oxford
- Odqvist FKG, Hult J (1962) *Kriechfestigkeit metallischer Werkstoffe*. Springer, Berlin u.a
- Orlová A, Buršík J, Kuchařová K, Sklenička V (1998) Microstructural development during high temperature creep of 9% cr steel. *Mater Sci Eng A* 245:39–48
- Penny RK, Mariott DL (1995) *Design for creep*. Chapman & Hall, London

- Perrin JJ, Hayhurst DR (1994) Creep constitutive equations for a 0.5Cr-0.5Mo-0.25V ferritic steel in the temperature range 600–675°C. *The. J Strain Anal Eng Des* 31(4):299–314
- Podgorny AN, Bortovoj VV, Gontarovskiy PP, Kolomak VD, Lvov GI, Matyukhin YJ, Morachkovskiy OK (1984) Polzuchest' elementov mashinostroitel'nykh konstruykij (Creep of machinery structural members, in Russ.). Naukova Dumka, Kiev
- Polcik P, Straub S, Henes D, Blum W (1998) Simulation of the creep behaviour of 9–12% CrMo-V steels on the basis of microstructural data. In: Strang A, Cawley J, Greenwood GW (eds) *Microstructural stability of creep resistant alloys for high temperature plant applications*. Cambridge University Press, Cambridge, pp 405–429
- Polcik P, Sailer T, Blum W, Straub S, Buršik J, Orlová A (1999) On the microstructural development of the tempered martensitic Cr-steel P91 during long-term creep - a comparison of data. *Mater Sci Eng A* 260:252–259
- Polmear IJ (1996) Recent developments in light alloys. *Mater Trans, Jpn Inst Met* 37(1):12–31
- Polmear IJ (2004) Aluminium alloys—a century of age hardening. *Mater Forum* 28:1–14
- Rabotnov YN (1963) O razrushenii vsledstvie polzuchesti (On fracture as a consequence of creep, in Russ.). *Prikladnaya Mekhanika I Tekhnicheskaya Fizika* 2:113–123
- Rabotnov YN (1969) Creep problems in structural members. North-Holland, Amsterdam
- Rauch M, Maile K, Seliger P, Reuter A, Tilsch H (2004) Numerische Berechnung und experimentelle Validierung der Schädigungsentwicklung in 9%-Chromstählen. 27. FVW/FVHT Vortragsveranstaltung, Langzeitverhalten warmfester Stähle und Hochtemperaturwerkstoffe, Stahlinstitut VDEh, Düsseldorf, pp 75–83
- Rieth M, Falkenstein A, Graf P, Heger S, Jäntsch U, Klimiankou M, Materna-Morris E, Zimmermann H (2004) Creep of the austenitic steel AISI 316 L(N). Experiments and models. Technical report, Forschungszentrum Karlsruhe, FZKA 7065, Karlsruhe
- Robinson DN, Binienda WK, Ruggles MB (2003) Creep of polymer matrix composites. I: Norton/Bailey Creep Law for transverse isotropy. *J Eng Mech* 129(3):310–317
- Röttger D (1997) Untersuchungen zum Wechselverformungs- und Zeitstandverhalten der Stähle X20CrMoV121 und X10CrMoVNb91. Dissertation, Universität GH Essen, Fortschr.-Ber. VDI Reihe 5, Nr. 507, Düsseldorf
- Sakane M, Tokura H (2002) Experimental study of biaxial creep damage for type 304 stainless steel. *Int J Damage Mech* 11:247–262
- Samir A, Simon A, Scholz A, Berger C (2005) Deformation and life assessment of high temperature materials under creep fatigue loading. *Materialwissenschaft und Werkstofftechnik* 36:722–730
- Segle P, Tu ST, Storesund J, Samuelson LA (1996) Some issues in life assessment of longitudinal seam welds based on creep tests with cross-weld specimens. *Int J Press Vessels Pip* 66:199–222
- Shibli IA (2002) Performance of P91 thick section welds under steady and cyclic loading conditions: power plant and research experience. *OMMI* 1(3). <http://www.ommi.co.uk>
- Simon A (2007) Zur Berechnung betriebsnah belasteter Hochtemperaturstähle mit einem konstitutiven Werkstoffmodell. Dissertation, Technische Universität Darmstadt, Berichte aus der Werkstofftechnik, Band 4/2007, Shaker Verlag Aachen
- Sklenička V, Kuchařová K, Svoboda M, Kloc L, Buršik J, Kroupa A (2003) Long-term creep behavior of 9–12% Cr power plant steels. *Mater Charact* 51(1):35–48
- Skrzypiek J, Ganczarski A (1998) Modelling of material damage and failure of structures. *Foundation of Engineering Mechanics*, Springer, Berlin
- Straub S (1995) Verformungsverhalten und Mikrostruktur warmfester martensitischer 12%-Chromstähle. Dissertation, Universität Erlangen-Nürnberg, VDI Reihe 5, Nr. 405, Düsseldorf
- Wohlfahrt H, Brinkmann D (2001) Consideration of inhomogenities in application of deformation models, describing the inelastic behaviour of welded joints. In: Steck E, Ritter R, Peil U, Ziegenbein A (eds) *Plasticity of metals: experiments, models, computation*. Final Report of the Collaborative Research Centre 319, Wiley-VCH, Weinheim, pp 361–382
- Wu R, Sandström R, Seitisleam F (2004) Influence of extra coarse grains on the creep properties of 9 percent CrMoV (P91) steel weldment. *J Eng Mater Technol* 26:87–94